Role of *L*-shell single and double core-hole production and decay in *m*-fold ($1 \leqslant m \leqslant 6$) photoionization of the Ar^+ ion

A. Müller[1,*] M. Martins[2] A. Borovik, Jr.[3] T. Buhr[3] A. Perry-Sassmannshausen[3] S. Reinwardt,[2] F. Trinter[4,5] S. Schippers[3] S. Fritzsche[6,7] and A. S. Kheifets[8]

[1]*Institut für Atom- und Molekülphysik, Justus-Liebig-Universität Gießen, 35392 Giessen, Germany*
[2]*Institut für Experimentalphysik, Universität Hamburg, 22761 Hamburg, Germany*
[3]*I. Physikalisches Institut, Justus-Liebig-Universität Gießen, 35392 Giessen, Germany*
[4]*Institut für Kernphysik, Goethe-Universität Frankfurt, 60438 Frankfurt am Main, Germany*
[5]*Molecular Physics, Fritz-Haber-Institut der Max-Planck-Gesellschaft, 14195 Berlin, Germany*
[6]*Helmholtz-Institut Jena, 07743 Jena, Germany*
[7]*Theoretisch-Physikalisches Institut, Friedrich-Schiller-Universität Jena, 07743 Jena, Germany*
[8]*Research School of Physics, The Australian National University, Canberra, ACT 2600, Australia*

(Received 25 July 2021; accepted 25 August 2021; published 9 September 2021)

Multiple ionization of the $Ar^+(3s^23p^5)$ ion by a single photon has been investigated in the photon-energy range 250–1800 eV employing the photon-ion merged-beams technique. Absolute partial cross sections were measured for all $Ar^{(1+m)+}$ product-ion channels with $1 \leqslant m \leqslant 6$ covering a size range from several tens of Mb down to a few b. Narrow $2p$-subshell excitation resonances were observed in all channels up to quadruple ionization at a photon-energy bandwidth of 52 meV. Double excitations involving a $2p$ and a $3s$ or $3p$ electron were also studied at high resolution and the measurements of the broad $2s$ excitation resonances directly showed their natural widths. Contributions of direct photo double ionization (PDI) to the production of the highest final Ar ion charge states are revealed, with PDI of the $2s$ subshell being mainly responsible for the production of Ar^{7+}. The experiment made use of the PIPE setup installed at beamline P04 of the PETRA III synchrotron light source of DESY in Hamburg. The measurements were supported by theoretical calculations to identify the main contributions to the observed cross sections. Comparisons of theory and experiment show remarkable agreement but also hint to additional ionization mechanisms that are not considered in the theoretical models such as core ionization accompanied by excitations with subsequent Auger decays leading to net m-fold ionization with $m \geqslant 4$.

DOI: 10.1103/PhysRevA.104.033105

I. INTRODUCTION

Interactions of photons with neutral atoms and molecules are receiving ever increasing attention [1] due to their fundamental nature and their importance in numerous applications. Steady improvement of brilliant light sources providing vacuum ultraviolet (VUV) and x-ray radiation at high intensities has facilitated substantial progress in many directions of photon science. One such direction is the extension of the target species in photon-matter interaction to electrically charged atoms and molecules. Ions can be produced in plasmas, generated by high-intensity laser shots or in a trap where atoms or molecules are exposed to high-density, energetic electron beams. In both scenarios, the ionic targets typically comprise several components at a time such as ions in different charge states. Absolute cross sections cannot generally be measured using these techniques ([2] and references therein).

Isotopically pure targets consisting of ions with given charge, mass, and energy can readily be made available in the form of an ion beam. However, the particle densities achievable in such a beam are typically below 10^6 cm^{-3} which is equivalent to a gas target at a pressure of several 10^{-8} Pa ($=10^{-10}$ mbar) and thus correspond to ultrahigh vacuum. The disadvantage of low-ion density in an ion beam can be partially overcome by employing a long photon-ion interaction length. The method of choice is the merged-beams technique [3] where the photon beam is coaxially immersed within an ion beam over a length that may reach more than 1 m. This technique can directly provide absolute cross sections for individual photo processes that lead to the removal of one or several electrons and it is also suitable for investigating fragmentation of target (molecular) ions.

While experiments on the detachment of negative ions require relatively low energies that can be provided already by lasers of visible and UV wavelengths [4,5], merged-beams studies on photoionization of positive ions were exclusively facilitated by the development of sufficiently brilliant synchrotron radiation sources. First merged-beams experiments on positive ions were limited to the measurement of cross sections greater than 5 Mb [6] where 1 b = 10^{-24} cm^2. The first two decades of experimental studies on photoionization of positive and negative ions following the pioneering work of Lyon *et al.* [7] on Ba^+ were comprehensively reviewed

*Alfred.Mueller@iamp.physik.uni-giessen.de

by Kjeldsen [8]. Since then, the sensitivity of merged-beams arrangements and the brilliance of available synchrotron radiation facilities were further improved [2,9,10]. With this study the lower limit of measurable cross sections has been pushed down to the level of 2 ± 1 b.

Multiple photoionization of ions is typically associated with small cross sections and requires comparatively high photon energies. Because of these reasons early experiments with ions concentrated on single ionization. With the construction of third-generation synchrotron light sources the situation started to change. In particular, merged-beams experiments with negative ions facilitated the observation of multiple detachment. Due to technical reasons these experiments did not provide access to single detachment and in most cases they were restricted to the observation of double detachment. However, the formation of high final charge states (up to fivefold detachment) was also observed ([11,12] and references therein). Along with the developments in multiple photodetachment of negative ions, measurements on multiple photoionization of positive ions have also become feasible [8,10,13–15].

Multiple photoionization of Ar ions has been studied previously by Blancard *et al.* [14] in the energy range 250–280 eV. Absolute cross sections for single, double, and triple ionization were measured at the SOLEIL synchrotron radiation facility for the Ar^+ ion. Covington *et al.* [16] investigated valence-shell single photoionization of Ar^+ in the energy range 27.4–60 eV. Single and multiple ionization of Ar^+ by electron impact has also been investigated [17–22]. Most recently, direct photo double ionization (PDI) of the Ar^+ M shell by a single photon in the energy range 60–150 eV has been addressed [23]. The experimental work by Covington *et al.* and Blancard *et al.* has stimulated theoretical investigations of photoionization of Ar^+ in which R-matrix techniques were employed [24].

Experimental results similar in nature to this work have been obtained for neutral Ar atoms. A wide energy range from 44 to 1300 eV was covered in relative ion-yield measurements by Saito and Suzuki [25]. The observed yields were then normalized to known total cross sections and thus put on an absolute scale. The energy resolution and energy step widths in this experiment were not sufficient to resolve fine details in the cross sections. And although a gas target could be employed with pressures $\approx 9 \times 10^{-4}$ Pa, the sensitivity of the measurements was relatively limited with the smallest observable cross sections (with uncertainties of about 50%) being of the order of 500 b. A detailed analysis of the results could not be provided due to the lack of suitable theoretical support.

The present project primarily aims at the detailed understanding of the influence of single and double L-shell vacancy formation in the photoabsorption by an Ar^+ ion. For this purpose all the accessible final charge states up to Ar^{7+} were measured with high precision and good accuracy. Comparison of the present experimental results with different theoretical calculations supports the determination of branching ratios for the decay of intermediate core-hole states in Ar^+, Ar^{2+}, and Ar^{3+} populated in single-photon absorption by an Ar^+ ion. It is worth noting that the present measurements starting from Ar^+ ions in their ground configuration can also be used to check previous experimental attempts [26,27] to determine the charge-state distribution of argon ions resulting from the removal of a $2s$ electron from neutral Ar. The excitation $2s \rightarrow 3p$ in the $Ar^+(3p^{-1})$ ion and the direct $2s$ ionization of neutral Ar produce the identical intermediate configuration $Ar^+(2s^{-1})$ that can subsequently decay by a multitude of different Auger processes and their combinations populating different final charge states up to Ar^{5+}. While the previous experiments employed coincidence Auger-electron spectroscopy to infer the final charge-state distribution of the decaying Ar^+ ion, the present results are based on the direct observation of the ionic product channels.

In a recent publication Wang *et al.* [28] presented a theoretical study on the cascade decay processes of the $1s$ core-hole state of the Ar^+ ion. The deexcitation trees were constructed by extensive level-to-level calculations. Inevitably, the decay of the initial K-shell vacancy populates levels with L- and M-shell holes which are relevant to this study on multiple photoionization of the Ar^+ ion near and above the L-shell ionization threshold. Hence, some of the predictions by Wang *et al.* on intermediate decay processes involving L-shell vacancies and occurring during decay cascades following K-shell ionization of the Ar atom may be tested by the present experimental results.

This paper is organized as follows. The Introduction is followed by a description of the experiment and the relevant experimental parameters. In the theory section three different kinds of calculations applied in the interpretation of the experimental data are briefly described: The Hartree-Fock method with relativistic corrections was used to obtain photoabsorption cross sections; the Jena Atomic Calculator (JAC) was applied to calculate level energies and transition rates; a recently developed theoretical model for the calculation of nonsequential photo double ionization was applied to obtain PDI cross sections for combinations of L- and M-shell electrons. The results section is divided in subsections discussing the total photoabsorption cross section of the Ar^+ ion, the average charge and individual charge-state fractions, branching ratios for the decay of vacancy levels populating different final charge states of the Ar ion, comparison of the experimental data for m-fold ionization with the results of theoretical calculations for single and double core-hole production by photoionization, and detailed spectra of single- and double-excitation resonances in the energy range 250 to about 350 eV. A summary and outlook section provides a brief overview of the main findings and implications of this project.

II. EXPERIMENT

The measurements were performed at the PIPE (Photon-Ion spectrometer at PETRA III) end station [9,29,30] of beamline P04 [31] at the PETRA III synchrotron radiation facility of DESY in Hamburg. The photon-ion merged-beams technique [3,32] was employed to obtain detailed photon-energy scans of ion yields resulting from net single and multiple photoionization of Ar^+ as well as absolute cross sections for the associated reaction channels. The experimental setup and procedures have been described in detail previously [29,30]. Here, a brief overview of the experimental

arrangement is given and details specific to the present measurements are provided.

The Ar^+ ions were produced in an electron-cyclotron-resonance (ECR) ion source. For this purpose Ar gas was leaked into the plasma chamber via a sensitive thermoelectrically controlled valve. Ions produced in the ECR plasma were extracted towards ground potential by a voltage of 6 kV and a beam of ions with different masses and charge states was formed. This beam was passed through an analyzing dipole magnet by which $^{40}Ar^+$ ions were selected. The isotopically pure $^{40}Ar^+$ beam was transported to an electrostatic spherical 50° deflector which merged the ion beam with the counter-propagating photon beam. Ions and photons could interact with one another over a length of 1.7 m. The ion beam was deflected from the photon-beam axis by the double-focusing demerger dipole magnet (bending radius $R_{\rm mag} = 1$ m) and collected in a large Faraday cup located inside the magnet chamber. The product ions were also deflected by the same magnet and directed towards the detector chamber that is mounted under an angle of 90° with respect to the photon beam axis [30]. Before entering the detector the product ions were deflected by 180° out of the horizontal plane in order to minimize background arising from stray charged particles or photons. The high-efficiency detector has been described in detail previously [33,34].

The demerger magnet generally allows one to select the mass and the charge state of the product ions so that individual reaction channels can be directly investigated, for example, by measuring the yield of certain product ions as a function of the photon energy. In the present case with Ar^+ parent ions, the product channels were defined by selecting and detecting the photoionized ions Ar^{2+}, Ar^{3+},..., Ar^{7+}. The associated absolute cross sections $\sigma_{1,m+1}$ for m-fold photoionization populating the final Ar ion charge states $Ar^{(1+m)+}$ with $m = 1, 2, \ldots, 6$ are determined from

$$\sigma_{1,m+1} = \frac{R_{m+1} q e v_{\rm ion}}{\varepsilon \phi_{\rm ph} I_{\rm ion} \mathcal{F}_L}, \tag{1}$$

where R_{m+1} is the $Ar^{(1+m)+}$ signal rate, q the initial ion charge state, e the elementary charge, $v_{\rm ion}$ the ion velocity in the photon-ion interaction region, ε the efficiency of the product-ion detector, $\phi_{\rm ph}$ the photon flux, $I_{\rm ion}$ the primary-ion current, and $\mathcal{F}_L$ the so-called form factor [3]. The photon flux is measured by using a calibrated photodiode. Due to the wide range of photon energies different gratings had to be employed and $\phi_{\rm ph}$ varied considerably. At about 250 eV, measurements were carried out at 19-meV resolution with a monochromator exit-slit setting of 20 μm and $\phi_{\rm ph} \approx 8 \times 10^{11}$ s^{-1}. At the same energy but with a 160-μm exit slit, the photon flux was $\phi_{\rm ph} \approx 10^{13}$ s^{-1}. The highest photon flux of almost 10^{14} s^{-1} was reached at about 600 eV with the exit slit opened to 1500 μm. At 1800 eV still more than 10^{12} s^{-1} could be obtained.

The Ar^+ parent-ion current $I_{\rm ion}$ depended on the degree of collimation. It reached up to 800 nA but was typically 300 to 600 nA during photon-energy scans. For the absolute measurements the ion beams were collimated more tightly to a diameter of at most 1 mm with a typical ion current $I_{\rm ion} \approx$ 25 nA. For determining the form factor $\mathcal{F}_L$ the interaction length L had to be defined and the beam overlaps [32] quantified. A drift tube with length $L = 50$ cm has been mounted along the photon-beam axis and centered at the object distance of the double-focusing demerger magnet. The interaction region was defined by applying a voltage to the drift tube so that ions changing their charge state inside the tube gain or lose kinetic energy by passing through the tube. In the present case −100 V were applied. The product ions $Ar^{(1+m)+}$ formed inside the interaction region thus experienced a net energy loss of $m \times 100$ eV. They were easily separated by the demerger magnet from the 6-keV ions produced outside the interaction region. By three movable pairs of horizontal and vertical slits mounted along the interaction region, the overlap of the photon and ion beams [29] was quantified and the form factor determined. Typical numbers obtained in the present absolute cross-section measurements were in the range $\mathcal{F}_L \approx$ 5000–7000 cm^{-1}.

Counting rates R_{m+1} ranged from several tens of thousands per second to about 1 in 40 seconds. The dark count rate of the detector was of the order of 0.02 Hz. Its efficiency for atomic particles like the present $Ar^{(1+m)+}$ ions is $\varepsilon = 0.97 \pm 0.03$ [34]. In order to obtain sufficient counting statistics for the experimental results described in this paper, about 42 shifts of 8 h each with photon beam on target were necessary.

The energy scale for the present measurements was particularly scrutinized because resonance positions obtained within this project showed a systematic deviation from resonance energies published previously by Blancard *et al.* [14]. The nominal (set) photon energies provided by the monochromator control system were compared with the $2p$ resonance energies measured for neutral Ar below the L edge, the C and O K edge $1s \rightarrow \pi^*$ resonances in neutral CO, the $1s \rightarrow \pi^*$ group of vibrationally resolved resonances in neutral N_2, and the near-K-edge region of neutral Ne. For this purpose, the P04 online diagnostic unit [35] was employed. In this unit, the photon beam is passed through an effusive gas target which is surrounded by 16 time-of-flight electron spectrometers all in a plane perpendicular to the photon-beam direction. At the center of the spectrometer arrangement the calibration gases are injected through a capillary. Electron count rates are recorded as a function of the set photon energy and, thus, the resonance spectra are obtained.

In the range 244 to 250 eV, the measured resonance energies were compared to the reference energies at the Ar L edge determined by King *et al.* [36]. At energies near 287.5 eV the first two carbon K-edge $1s \rightarrow \pi^*$ resonances in neutral CO were observed and their energies compared to the literature values of Tronc *et al.* [37]. Near 400 eV the $1s \rightarrow \pi^*$ group in neutral N_2 was measured with high resolution and compared to the results of Sodhi and Brion [38]. Around 534 eV the oxygen K-edge $1s \rightarrow \pi^*$ resonances in neutral CO were measured and their energies compared to the results of Sodhi and Brion [38]. The K-edge region of neutral Ne was scanned in the energy range 865–870 eV and the results were compared to the corrected data obtained previously by Wuilleumier [30,39].

The differences ΔE between the resonance energies observed at the beamline and the reference energies from the literature could be described by a linear function of the photon energy $E_{\rm ph}$ ($\Delta E \approx 0.16$ eV $- 6.6 \times 10^{-4} \times E_{\rm ph}$, energies in eV). The energy scale of the present measurements was

calibrated accordingly. In addition, the Doppler effect caused by the velocity of the ions towards the incoming photons [40] was corrected for.

The uncertainty of the present experimental energy scale is mainly determined by the uncertainties quoted for the reference energies from the literature. They are 10 meV at about 244 eV, 20 meV at about 287 eV, 20 meV at about 400 eV, 90 meV at about 534 eV, and 200 meV [30] at about 867 eV. Considering that the uncertainties claimed in the literature are often overly optimistic [30,40], an uncertainty of the $2p \rightarrow n\ell$ transition energies of 30 meV is estimated for the narrow absorption resonances occurring in the Ar^+ ion in the energy range from 250 to 265 eV.

The systematic uncertainties of cross sections obtained by merged-beams experiments at the PIPE setup have been discussed in detail previously [29]. The total systematic uncertainty is estimated to be 15%. Statistical uncertainties vary substantially depending on the final ionization channel observed. The statistical uncertainty can be at or below the level of 0.1% at the peaks of strong resonances and may be larger than 50% for small cross sections, e.g., in the threshold region of sevenfold ionization.

III. THEORY

A. HFR calculations

The Ar^+ L-shell photoabsorption cross sections for the $^2P_{3/2}$ and $^2P_{1/2}$ initial states were modeled by *ab initio* configuration-interaction (CI) calculations on the basis of the Hartree-Fock method with relativistic extensions (HFR) applying the Cowan code [41]. The theoretical approach has been described in detail previously [42] in connection with the $2p$-shell excitation of atomic chlorine which is isoelectronic with the Ar^+ ion.

For describing the Ar^+ ground state, the CI expansion was chosen to include the excited configurations $3s^23p^3n\ell^2$ (with $n\ell^2 = 3d^2, 4s^2, 4p^2$), $3s^23p^44p$, and $3s^13p^53d^1$ in addition to the initial configuration $3s^23p^5$.

The direct photo single-ionization cross sections for the removal of a $3p$ or a $3s$ valence electron and for the ionization of a $2p$ or a $2s$ inner-shell electron were calculated from the dipole matrix elements $\langle\Psi_{\epsilon\ell}|er|\Psi(^2P_{3/2,1/2})\rangle$ for the $^2P_{3/2}$ and $^2P_{1/2}$ initial levels. The wave function $\Psi_{\epsilon\ell}$ represents the residual Ar^{2+} ion and the ionized electron with kinetic energy ϵ and angular momentum $\ell = s, p, d$. Due to the open $3p$ shell in Ar^+ this results in different ionization thresholds corresponding to the different possible LS terms of the core-excited Ar^{2+} ion which can be seen, e.g., in Fig. 16 for the case of $2p$ ionization (resulting in $2p^53s^23p^5\epsilon\ell$ final states).

The configurations included in the CI expansion for describing the $2p^{-1}$ core-excited states are given in Table I. Single, double, and higher multiple excitations of $3s$ and $3p$ electrons are taken into account. For single excitations, Rydberg orbitals ns and $n'd$ with principal quantum numbers n up to 6 and n' up to 5 are included. Double excitations are accounted for by including configurations where either an additional $3s$ or an additional $3p$ electron is excited into a $3d$, $4s$, or $4p$ orbital. Furthermore, multiple excitations are added in the cross-section calculations by promoting two or three $3s$ or $3p$ electrons into $3d$, $4s$, and $4p$ orbitals. All possible LS levels from these configurations are taken into account.

TABLE I. List of configurations used in the HFR-CI calculations.

Single excitations
$[2s^22p^53s^23p^5](3d^1, 4d^1, 5d^1, 4s^1, 5s^1, 6s^1)$; $2s^12p^63s^23p^6$; $2s^12p^63s^23p^54p^1$; $2s^12p^63s^23p^55p^1$; $2s^12p^63s^23p^56p^1$
Double excitations
$2s^22p^53s^23p^33d^3$; $2s^22p^53s^13p^53d^2$; $2s^22p^53s^13p^54s^2$; $2s^22p^53s^13p^64p^1$; $2s^22p^53s^23p^43d^14p^1$; $2s^22p^53s^23p^44s^14p^1$
Multiply excited configurations
$2s^22p^53s^13p^43d^24p^1$; $2s^22p^53p^43d^34p^1$; $2s^22p^53s^13p^44s^24p^1$; $2s^22p^53s^13p^43d^14s^14p^1$; $2s^22p^53p^43d^24s^14p^1$

For the $2s^{-1}$ excitation resonances, a smaller CI expansion without double and multiple electron excitations has been used to keep the overall calculations manageable which include all possible Auger decays of the excited levels populated in the calculations. The linewidths of the resonances are calculated from the lifetime of the core-hole resonances resulting from the Auger transition rates into various final doubly charged ionic states. The Auger lifetimes have been calculated for all singly and doubly excited states calculating the LM_1M_1, $LM_1M_{2,3}$, and $LM_{2,3}M_{2,3}$ spectator and $LM_{2,3}X$, LM_1X ($X = 3d$-$5d, 4s$-$6s, 4p$) participator Auger transition rates into $\epsilon(s, p, d, f)$ electron continua. The direct $3s$ and $3p$ ionization is also included for these channels. For the direct $2p$ ionization the $2p^53s^23p^5\epsilon(sd)$ and $2p^53s^23p^44p\epsilon(sd)$ channels are taken into account. The typical line widths calculated from the Auger transition rates are of the order of 20 meV for the $2p$ core-hole levels. They are significantly larger (up to several eV) for the $2s$ core-hole levels because these can decay via fast $L_1L_{2,3}M$ Coster-Kronig processes. The HFR calculations result in cross sections for nonresonant and resonant photoabsorption by the Ar^+ ion.

B. Modeling atomic cascades

To model the relaxation of inner-shell excited or ionized atoms, detailed computations of the level structure and transition rates are needed for different charge states in order to predict all the resonance energies, thresholds, or even final ion charge-state distributions. Such cascade computations were performed using the flexible toolbox provided by the Jena Atomic Calculator (JAC) that integrates different processes within a single framework and ensures good (self-)consistency of generated data. The JAC toolbox [43] is based on the multiconfiguration Dirac-Hartree-Fock (MCDHF) method [44,45] and, hence, is suitable for atoms and ions with rather arbitrary shell structures as well as for describing numerous atomic processes. This toolbox is based on Julia, a relatively new programming language for scientific computing, that brings together high performance and productivity in developing such tools [46]. Below, we make use of the JAC toolbox to calculate the energies, lifetimes,

and branching ratios needed to estimate ion distributions following the relaxation of inner-shell vacancies produced in different excitation and ionization processes that contribute to the total photoabsorption by Ar^+ ions.

To analyze atomic cascades more systematically, JAC has recently been enlarged for modeling different *cascade schemes*, i.e., relaxation scenarios, such as the stepwise decay of an (inner-shell) excited atom via photon or electron emission [47]. In JAC, the implementation of these cascade schemes is based on so-called pathways, which refer to sequences of two or more levels, and how they are subsequently occupied in the course of the relaxation. Obviously, a very large number of such pathways may naturally occur in the deexcitation of deep inner-shell holes. For a stepwise decay of an atom or ion, we start from either one or a few excited electron configurations which then decay by different user-selected atomic processes, including autoionization and photon emission, until a given number of electrons is released and/or the ions cannot further decay to any lower level.

In practice, the large number of different measurements and observations in studying atomic relaxation processes makes it unfeasible to implement *cascade models* for each individual experiment or setup separately. Moreover, from a physics viewpoint, many of these observations, e.g., photon, electron, or ion distributions, can be readily traced back to the same single-step processes and, hence, make a recalculation of the underlying amplitudes unnecessary. In JAC, we therefore distinguish between cascade *computations* and *simulations* [47]. While the cascade computations are performed with the goal to calculate and *compile* the many-electron amplitudes and rates for all steps of the cascade, the simulations then make use of these (precompiled) data in order to derive the ion, photon, or electron distributions, or any other information, if needed.

In Sec. IV, the results of such cascade simulations are presented. The calculations were performed to estimate the ion distributions resulting from different inner-shell excitations. Because of the complexity of these cascades, however, the quantum-mechanical representation of the fine-structure levels needs to be simplified quite drastically by reducing the amount of interelectronic interactions accounted for in the calculations. Often, several tens of thousands or even more transition amplitudes are required already for a midsize cascade in contrast to most standard atomic-structure calculations. To establish a hierarchy of useful approximations, JAC therefore differentiates between several cascade *approaches* for the representation of the atomic state functions (ASF) involved. For Ar^+, unfortunately, we were only able to apply the simplest, i.e., the so-called average single-configuration approach, in which all ASF are approximated by single-configuration state functions (CSF) and by the orbitals of the initial levels. This approach neglects all configuration mixing between the bound-state levels and restricts the computations to just the Coulomb interaction among the electrons as well as a single set of continuum orbitals for each *step* of the cascade [48]. These limitations are likely the main reason for the discrepancies of the predicted ion distributions, when compared with the measurements.

Until the present time, the main focus in developing JAC has been placed on the integration of a large number of atomic processes and cascades in order to describe atomic behavior within different environments. As discussed at length in the description of the code [49], an improved representation of the fine-structure levels will allow for more detailed cascade simulations in the future.

C. Modeling direct photo double ionization

Direct, or simultaneous, ejection of two electrons from an atom by a single photon is facilitated by two principal mechanisms [50]. In the so-called two-step one (TS1) mechanism, the primary photoelectron is ejected and, on its way out, it knocks off a secondary photoelectron. The alternative shake-off (SO) mechanism is the result of the sudden removal of the photoelectron and the associated change of the effective core charge for the other electrons. With a certain probability, one of these electrons may be shaken off to the continuum.

The presently employed theoretical model treats the TS1 mechanism as described in detail in [51]. In the present application, the model considers the TS1 process as a sequence of the single photoionization of Ar^+ followed by electron-impact ionization of the residual Ar^{2+} ion. The approximation is made that the energy is conserved between these two stages while the virtual ionization and excitation processes are ignored:

$$\sigma^{2+}_{\gamma,2e}(\omega) = \sigma^{+}_{\gamma,e}(\omega) \times \sigma_{e,2e}(\omega - I_p). \tag{2}$$

Here I_p is the ionization potential for removal of the primary photoelectron. The cross sections are labeled by the incident projectile (the photon γ or electron e) and the number of ejected electrons (for single e and double $2e$ ionization channels). Unlike in the earlier theoretical works [52–54], which employed the lowest-order perturbation theory, the present theory is not perturbative. It includes many-electron correlations both in the single photoionization and the electron-impact ionization calculations. The $\sigma^{+}_{\gamma,e}(\omega)$ term is evaluated using the random-phase approximation with exchange (RPAE) [55]. The $\sigma_{e,2e}(E)$ term is calculated by solving the integral equation for the reducible self-energy part of the one-particle Green's function [56] in the single-dipole channel:

$$\sigma_{e,2e}(E) = \mathrm{Im}\,\Sigma_{J=1}(E). \tag{3}$$

Numerical implementation of the RPAE and inelastic scattering (SCAT) techniques is provided by the ATOM suite of programs [57].

The present theoretical approach is applicable both to neutral and electrically charged atoms. The accuracy of the calculations is expected to be somewhat reduced in cases where electron correlations are particularly important, e.g., in processes involving the valence shells of negative ions or neutral atoms. A comparison of the present theory for valence-shell PDI of neutral Ar with experiments shows quite reasonable agreement, with minor deficiencies in the low-energy region. For positive ions and especially with increasing ion charge states, the outer-shell electrons are more tightly bound by the Coulomb field of the ionic core and the role of many-electron correlation decreases. This diminishes the effect of the virtual intermediate states that do not conserve energy and are neglected in the present model.

As a result, the accuracy of the calculations for the Ar^+ ion should be quite satisfactory as demonstrated for the M-shell PDI of Ar^+ [23].

For the present Ar^+ L-shell photoionization project, cross sections for PDI were calculated for all possible pairs of electrons with one from the $2s$ and $2p$ subshells and one from the $2s$, $2p$, $3s$, or $3p$ subshells. For the combination of one electron from the $2s$ and one from the $2p$ subshell the present model gives different results for the combinations $2s + 2p$ and $2p + 2s$ depending on whether the $2s$ or the $2p$ electron absorbs the incoming photon. Within the present PDI model, the total cross section for the removal of one electron from the $2s$ and one from the $2p$ subshell is given by the sum of the two contributions $2s + 2p$ and $2p + 2s$.

IV. RESULTS

A. Photoabsorption: Experiment and theory

In the present experiments, absolute partial cross sections $\sigma_{1,m+1}$ for m-fold photoionization of Ar^+ were measured with m ranging from 1 to 6. In the investigated energy range 250 to 1800 eV the excitation of the parent ion produces at least one vacancy in the L shell. The relaxation of such a vacancy by photon emission is very unlikely in comparison with the probabilities for Auger decays. Without any change of the parent-ion charge state, it leads to Ar^+ product ions and emitted photons, which is an absorption channel that could not be observed in the present experiments. Cascade calculations employing JAC (see Sec. III B) predict branching ratios between 0.0013 and 0.017 for the radiative stabilization of the $2p$ vacancy levels produced in the Ar^+ ion by the excitation of a $2p$ electron to the $3d$ subshell. The present experiments could address the production of charge states up to Ar^{7+} but showed no measurable signal of Ar^{8+} so that it is safe to assume that the total absorption cross section of the Ar^+ ion can be well represented by $\sigma_{\rm abs} = \sum_{m=1}^{6} \sigma_{1,m+1}$.

The stacked sum of the partial photoionization cross sections is shown on a logarithmic scale in Fig. 1 as a function of the photon energy $E_{\rm ph}$. In order to emphasize the low-energy region especially in the range 250–270 eV where sharp resonances occur in the absorption spectrum, the difference $E_{\rm ph} - 249\,{\rm eV}$ is shown on a logarithmic scale, as well. The first tick labeled 1 thus corresponds to $E_{\rm ph} = 250\,{\rm eV}$.

The range of the partial cross sections $\sigma_{1,m+1}$ measured within this project spans approximately eight orders of magnitude. Statistical uncertainties cause the noisy character of the smallest cross sections. In the single, double, triple, and quadruple ionization at energies below 270 eV, spectra of partly resolved narrow resonances are seen that are associated with excitations of a $2p$ electron to one of the possible levels in the M, N, O, ... principal shells. The measurements in the energy range up to 270 eV were performed at a photon-energy bandwidth of 52 meV. At higher energies up to 300 eV the resolving power was reduced. However, the structures in the cross sections were identical for bandwidths between 52 and 175 meV. Resonances at yet higher energies associated with excitation of a $2s$ electron have widths of more than 2 eV and were measured at energy spreads not exceeding 400 meV. As a consequence of these findings, the cross sections presented here for photoabsorption by the Ar^+ ion may be considered as the results of measurements all taken at 52 meV photon-energy spread. Details of the shapes of the measured cross sections are discussed in the following subsections where also the physical mechanisms causing the specific energy dependencies of the partial cross sections are elucidated.

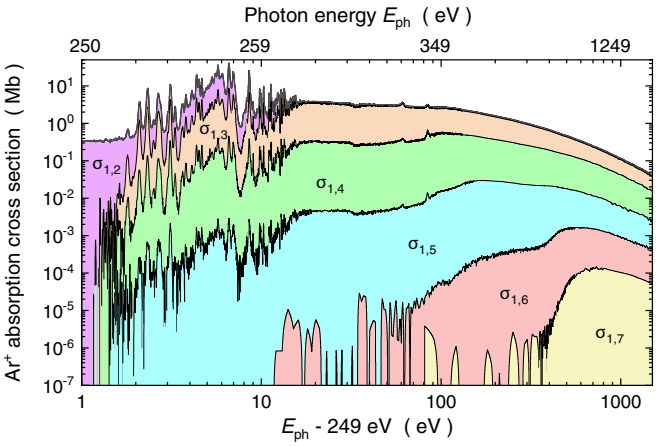

FIG. 1. Overview of the experimental results. The total photoabsorption cross section of the Ar^+ ion in the energy range 250 to 1800 eV is shown as the sum of the individual stacked contributions $\sigma_{1,m+1}$ of single ($m = 1$) and multiple ($m = 2, 3, 4, 5, 6$) photoionization. The subscript "$1, m + 1$" characterizes the initial and final charge states of the Ar ion. The contributions of the different partial cross sections to the overall sum, i.e., the photoabsorption cross section, are differently shaded and appropriately labeled.

Figure 2 shows a comparison of the present experimental photoabsorption cross section with the measurement

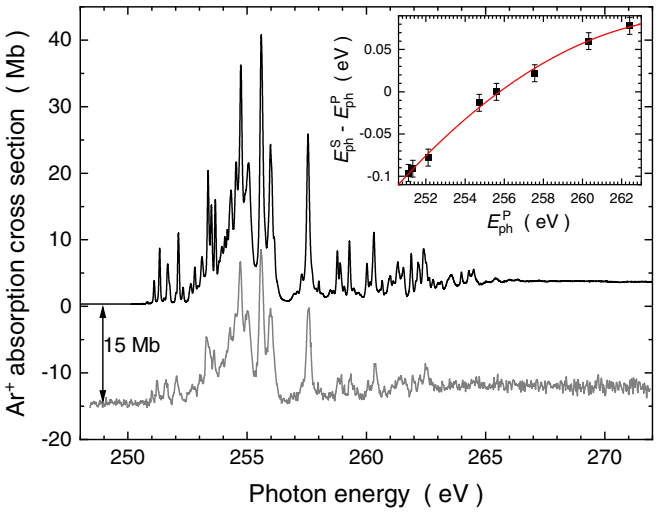

FIG. 2. Comparison of the present total experimental photoabsorption cross section (solid black line) of the Ar^+ ion with the result of Blancard *et al.* [14] (solid gray line). The latter curve has been vertically offset by −15 Mb to allow for easier comparison. The inset shows the systematic deviation of resonance energies $E_{\rm ph}^S$ obtained by Blancard *et al.* at SOLEIL and the present energies $E_{\rm ph}^P$ obtained at PETRA III. The solid curve in the inset is a fit to the experimental energy differences.

published by Blancard *et al.* [14]. Apart from the higher resolution of the present measurement (52 meV photon-energy spread versus 140 meV) and the resulting differences in peak heights, the two spectra are very similar. A closer look reveals that the absorption cross section measured by Blancard *et al.* at 270 ± 1 eV is 2.92 Mb while the present result is 3.73 Mb. The ≈22% difference of the previous measurement from the present one is well within the combined mutual uncertainties. However, a previous comparison with R-matrix calculations by Tyndall *et al.* [24] suggested that the cross sections measured by Blancard *et al.* are slightly too low. This observation is supported by the present theoretical results (see below).

The inset in Fig. 2 reveals a systematic deviation of the energy axes of the present experiment at PETRA III and the measurements by Blancard *et al.* [14] which were carried out at the SOLEIL synchrotron radiation facility. The associated energies of selected resonances are at $E^P_{\rm ph}$ in the present PETRA III experiment and at $E^S_{\rm ph}$ in the previous experiment at SOLEIL. The inset shows differences $E^S_{\rm ph} - E^P_{\rm ph}$ as a function of $E^P_{\rm ph}$. Over an energy span of about 10 eV the overall deviation between the two data sets is almost 180 meV. On the basis of the careful and repeated energy calibration of the present measurements we believe that the uncertainty of the photon-energy axis in the experiments of Blancard *et al.* is larger than quoted. The uncertainty of the present energy axis is estimated to be ±30 meV, the quoted uncertainty of the Blancard *et al.* energies is ±40 meV.

For understanding the structures observed in the measured cross sections for m-fold photoionization it is elucidating to take a closer look at threshold energies of processes that can contribute. Table II shows calculated threshold energies for the removal of one or two electrons from the L and M shells of the Ar^+ ion. Subshell vacancies listed in the first column of the table are produced by direct single or double ionization or by single ionization plus excitation. The second column provides the energy ranges of the levels within each associated vacancy configuration. The level energies were calculated employing JAC. The fourth column is based on calculations with the Cowan code in HFR approximation and is meant to provide a reference for assessing the reliability of the present JAC results. The accuracy of these JAC calculations is expected to be of the order of few eV. The third column shows the threshold energies obtained from the PDI model. In this theory, fine-structure effects are not considered and, therefore, the threshold energies are configuration-averaged energy differences. The calculated PDI energies are typically at the high end of the present JAC level-energy ranges.

Theoretical approaches towards photoionization of atoms primarily determine the photoabsorption cross section. At relatively low photon energies, that are just slightly above the lowest ionization energy, the cross sections for absorption and single ionization are almost identical. In the present case, where multiple ionization plays an important role, the results of the theoretical calculations have to be compared to the experimentally determined absorption cross section. For the present energy range, two separate R-matrix calculations have been published [24,58], the more recent work being restricted to energies below 270 eV. Photoabsorption by Ar^+ ions was also calculated within the previous L-shell photoionization study of Blancard *et al.* [14]. The results were restricted to the energy range 248 to 272 eV. Within the present project, calculations have been performed using the HFR approach described in Sec. III A. The cross sections calculated in great detail for energies up to 445 eV are complemented with simpler calculations covering direct single ionization for removing an electron from one of the subshells of the L or M principal shells. PDI of the M and L shells provides only a very minor contribution to the total absorption cross section.

TABLE II. Threshold energies of processes that may contribute to the present multiple-ionization cross sections of the $Ar^+(3s^2 3p^5)$ ion. The energies are given in eV relative to the ground level of the parent Ar^+ ion. JAC stands for the Jena Atomic Calculator. The PDI model calculations provide configuration-averaged energies, while the other calculations yield level-to-level energy differences. In the table the lowest and highest excitation energies within the different vacancy configurations are given. Direct single ionization of subshell $n\ell$ produces a vacancy $n\ell$. Direct single ionization of subshell $n\ell$ plus excitation $n'\ell' \rightarrow n''\ell''$ is characterized by $n\ell, n'\ell' \rightarrow n''\ell''$ in the first column. PDI of subshells $n\ell$ and $n'\ell'$ is characterized by $n\ell, n'\ell'$ in the first column.

Subshell vacancies	JAC	PDI model	Cowan code
$2p$	262.1–269.2	274	262.8–270.1
$2p, 3p \rightarrow 3d$	279.0–299.7		281.3–300.7
$2p, 3p \rightarrow 4s$	284.1–296.5		287.3–297.8
$2p, 3p$	305.2–321.1	319	306.7–317.1
$2p, 3s$	324.3–341.5	339	326.3–339.1
$2s$	344.4–345.4	349	343.6–344.0
$2s, 3p$	393.2–399.7	395	387.4–393.8
$2s, 3s$	403.2–424.5	414	405.1–415.1
$2p, 2p \rightarrow 3p$	522.7–544.4		522.3–539.9
$2p, 2p \rightarrow 3d$	542.2–578.6		541.3–574.9
$2p, 2p \rightarrow 4s$	551.3–575.8		549.4–569.8
$2p, 2p$	567.5–587.6	593	569.2–589.5
$2s, 2p$	637.0–666.2	668	639.7–668.2
$2s, 2s \rightarrow 3p$	683.9		685.0
$2s, 2s \rightarrow 3d$	705.0–718.3		705.8–719.7
$2s, 2s \rightarrow 4s$	715.1–715.6		714.3–714.8
$2s, 2s$	732.1–732.4	741	734.1–734.3

Calculated PDI cross sections are shown in Fig. 3 for all combinations of two electrons, one from either subshell $2s$ or $2p$ and one from subshells $2s$, $2p$, $3s$, or $3p$. The sum of all individual cross sections $\sigma_{2s,2s}$, $\sigma_{2s,2p}$, $\sigma_{2p,2p}$, $\sigma_{2s,3s}$, $\sigma_{2s,3p}$, $\sigma_{2p,3s}$, and $\sigma_{2p,3p}$ is less than a few percent of the experimentally derived total photoabsorption cross section of Ar^+. Considering the systematic 15% uncertainty of the experimental cross sections, the PDI contributions can be neglected in the theoretical modeling of the total absorption cross section as far as the comparison with the present experimental data is concerned.

Figure 4 shows a comparison of the total experimental absorption cross section with the results of theoretical calculations that do not comprise PDI. Only those theoretical results are displayed that cover the whole energy range up to 1800 eV. The R-matrix calculation by Witthoeft *et al.* [58] does not reproduce the resonance features well. However, the overall smooth parts of the cross section agree with the

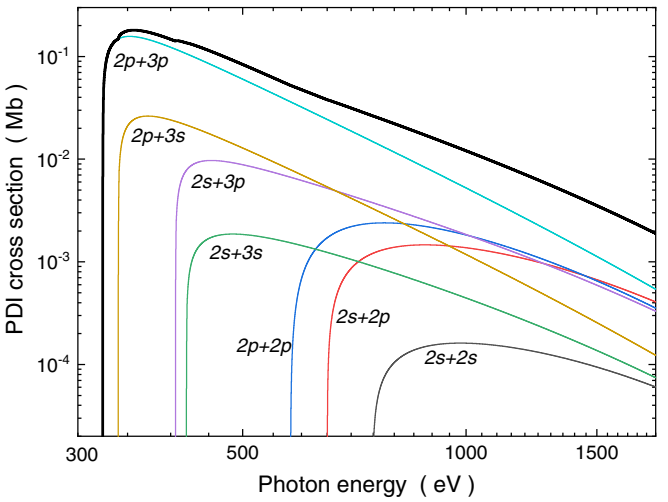

FIG. 3. Calculated cross sections $\sigma_{n\ell,n'\ell'}$ ($n = 2$, $n' = 2, 3$, and $\ell, \ell' = 0, 1$) for PDI of the Ar^+ ion involving one or two L-shell electrons. The combinations of electron subshells $n\ell, n'\ell'$ are indicated for each cross section. The thick solid black line is the sum of all PDI contributions.

experiment, given the uncertainty of the measured cross sections. The detailed HFR calculations are much better in reproducing the fine details of the absorption cross section (see also Figs. 5 and 6). The resonances associated with $2s \rightarrow 3p$ and $2s \rightarrow 4p$ excitations at ≈310 eV and ≈333 eV, respectively, also show satisfactory agreement of the detailed HFR theory with the experiment. The simpler HFR calcula-

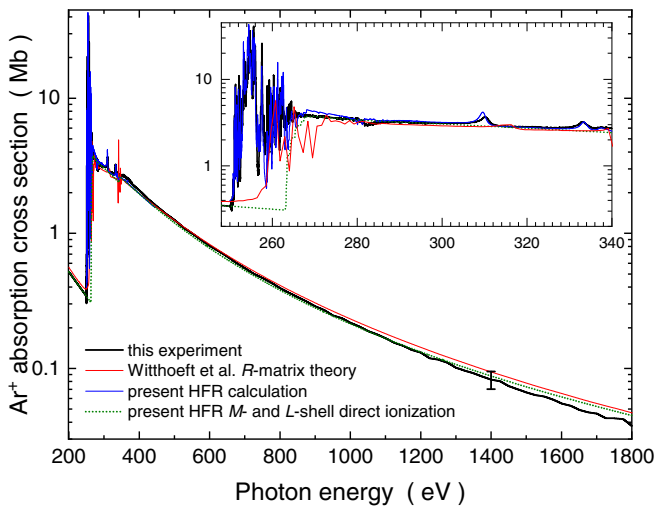

FIG. 4. Comparison of the total experimental photoabsorption cross section of the Ar^+ ion with the results of theoretical calculations. The present experimental results are shown as a thick solid line. The R-matrix results of Witthoeft *et al.* [58] are represented by a light (red) thin solid line. The present detailed HFR results including resonances are shown as the dark (blue) solid line. The HFR cross sections for direct single ionization of the M and L shells are displayed as a dotted (green) line. The error bar on the experimental curve at 1400 eV depicts the systematic uncertainty of the present measurements. The inset shows a blowup of the main graph in the energy range 248 to 340 eV.

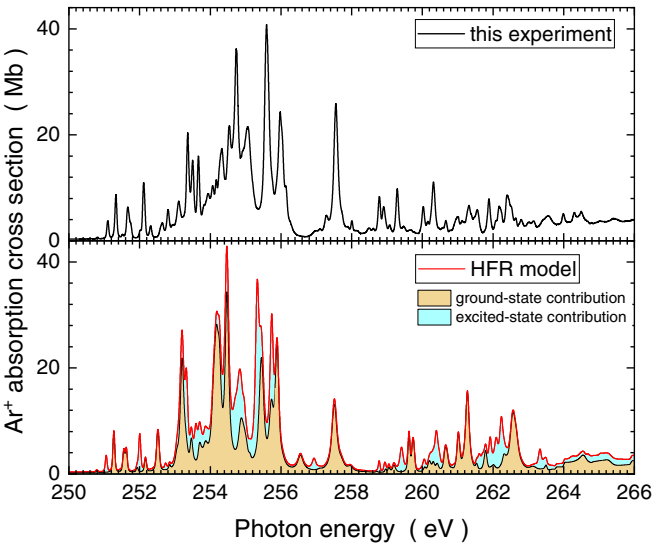

FIG. 5. Comparison of the total experimental photoabsorption cross section of the Ar^+ ion (upper panel) with the results of the present HFR calculations (lower panel). The experimental results were obtained at 52-meV photon-energy bandwidth. The theoretical contributions (convoluted with a 52-meV FWHM Gaussian) for the ground level and the associated metastable upper fine-structure level are plotted in a stacked graph with different shadings for the parent-ion states. The overall contributions of the metastable level, shown by the lighter (cyan) shading, are relatively small. The theoretical energy axis $E_{\rm ph}^{\rm theo}$ was adjusted to the experiment by applying the linear transformation 2.875 eV + 0.9865 × $E_{\rm ph}^{\rm theo}$ to the theoretical energy axis.

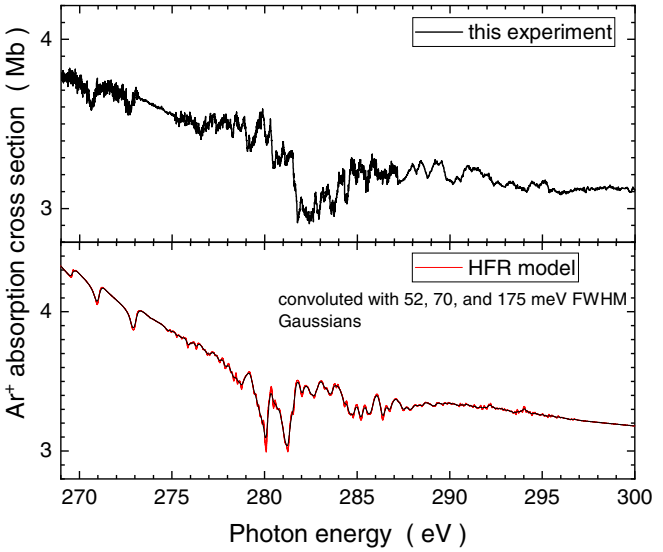

FIG. 6. Comparison of the total experimental photoabsorption cross section of the Ar^+ ion (upper panel) with the results of the present HFR calculations (lower panel). The experimental results were obtained at different photon-energy bandwidths between 52 and 175 meV. As in Fig. 5 the theoretical curve is a weighted sum of the contributions of the ground level and the associated metastable upper fine-structure level. The theory result was convoluted with Gaussians of different widths as indicated in the lower panel without significant differences between the resulting curves. The theoretical energy axis was transformed in the same manner as in Fig. 5.

tions that are restricted to direct single photoionization of the Ar^+ ion do not include resonance contributions and therefore cannot reproduce the $2p$ and $2s$ excitations seen in the experiment. However, they are in good overall agreement with the measured cross-section function outside the relatively narrow resonance regions.

The Ar^+ ion beam used in the experiment consists of ions in the $3s^2 3p^5$ ground configuration. The associated ^2P term involves two fine-structure levels with the total angular momentum quantum number $J = \frac{3}{2}$ for the ground level and $J = \frac{1}{2}$ for the metastable excited level with an excitation energy of 0.177 eV [59]. The ion source with its radio-frequency-heated electrons certainly produces ions in both levels. It is reasonable to assume a statistical population of the two fine-structure levels. The detailed HFR calculations provide the absorption cross sections for each of these levels separately. For comparison with the experiment a weighted sum of the two contributions is calculated with a weight of $\frac{2}{3}$ for the $J = \frac{3}{2}$ and $\frac{1}{3}$ for the $J = \frac{1}{2}$ component. The two contributions are shown by different shadings in the stacked plot of the calculated absorption cross section in the lower panel of Fig. 5. The darker (orange) shading shows the contribution of the ground level, the lighter (cyan) shading of the cross section, plotted on top of that, marks the contribution of the excited fine-structure level. For comparison, the upper panel shows the experimentally determined absorption cross section measured at 52-meV energy resolution. The theory results were accordingly convoluted with a Gaussian of 0.052-eV full width at half-maximum (FWHM). Theory and experiment are in remarkable agreement.

The resonances displayed in Fig. 5 are associated with $2p$ excitations to ns, nd levels with principal quantum numbers $n \geqslant 3$. The lowest $2p$ ionization threshold of the ground-state Ar^+ ion is expected at 262.8 eV according to the HFR calculations and at 262.1 eV according to the JAC calculations. The highest threshold for populating a level within the $2s^2 2p^5 3s^2 3p^5$ configuration with a $2p$ electron removed from the $2p$ subshell of Ar^+ is predicted by the present JAC calculation to be at 269.2 eV (270.1 eV according to the HFR calculations). Thus, at energies above approximately 270 eV and below the $2s$ excitation threshold at about 310 eV, all resonances in the measured absorption cross section must be due to multiple excitations, most likely double excitations involving one $2p$ and one $3p$ or $3s$ electron. Figure 6 displays the absorption cross section of Ar^+ in the energy range 269 to 300 eV where such double-excitation resonances were found in the experiment and in the detailed HFR calculations.

Two distinct window resonances at experimental photon energies ≈270.6 eV and ≈272.6 eV are seen in both the measured and the calculated cross sections. These resonances are slightly shifted to higher energies (by approximately 0.25 eV) in the calculations but are well reproduced in size relative to the experiment. These window resonances are most likely due to interference of $2s^2 2p^6 3s^2 3p^5 \rightarrow 2s^2 2p^5 3s^1 3p^6 4p$ double excitations and $2p$ direct ionization with their subsequent Auger decays. Their energy difference of approximately 2 eV corresponds to the fine-structure splitting of the $2p^{-1}\ ^2P_{1/2,3/2}$ core vacancy. At energies between 279 and 288 eV strong window resonances are observed both in the measured spectrum and in the HFR calculations. They are probably related to double excitations to $2s^2 2p^5 3s^2 3p^4 3d 4p$ or $2s^2 2p^5 3s^2 3p^4 4s 4p$ configurations. Perfect agreement of theory and experiment in such a complex mixture of numerous resonances cannot be expected, given the uncertainties in calculated energies. However, the magnitudes of double-excitation resonances and their approximate energies are well reproduced by the HFR calculations.

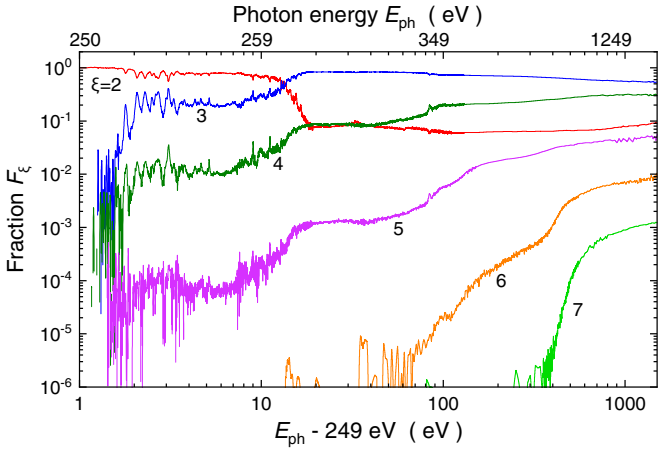

FIG. 7. Fractions F_ξ of $Ar^{\xi+}$ product ions in charge states $\xi = 2, 3, \ldots, 7$ observed after absorption of a photon (with a given energy E_{ph}) by the Ar^+ ion (see text).

B. Charge-state fractions, branching ratios for $2p$-hole decays, and average product-ion charge

When an energetic photon is absorbed by an atom, one or possibly several electrons are released. This is obviously also true when the absorber is an Ar^+ ion. In the present experiment the charge state of each product ion is measured approximately 6 μs after the absorption of the photon. This time span is sufficiently long for the intermediate, highly excited ion to completely relax and populate its final charge state. The relative abundance or fraction F_ξ of $Ar^{\xi+}$ product ions in charge state ξ is given by $F_\xi = \sigma_{1,\xi}/\sigma_{abs}$. The fractions F_ξ obtained in the present experiment are displayed in Fig. 7.

The lowest energy necessary to excite an L-shell electron from the ground configuration of Ar^+ is experimentally found at about 250.8 eV. Immediately below that energy, direct single ionization of the M shell determines the absorption cross section. Hence, the average final charge state is $\xi = 2$ and the associated fraction F_2 is 1 for energies below 250.8 eV. Even at about 100 eV where the cross section for direct M-shell double ionization reaches its maximum of ≈70 kb [23], F_2 is expected to be greater than 0.95. As soon as a vacancy in the L shell can be produced, the fraction F_3 increases and the resonant character of L-shell excitation causes rapid variations of all fractions F_ξ with $\xi = 2, 3, 4, 5$ that are influenced by the presence of an initial L-shell vacancy. At a photon energy of about 270 eV, the cross section for direct single $2p$-subshell ionization reaches its maximum. There, the fraction F_2 goes to approximately 0.08 and $F_3 \approx 0.85$ dominates the charge-state distribution. With increasing photon energy an increasing number of reaction channels open up and the higher charge states up to $\xi = 7$ show steep increases.

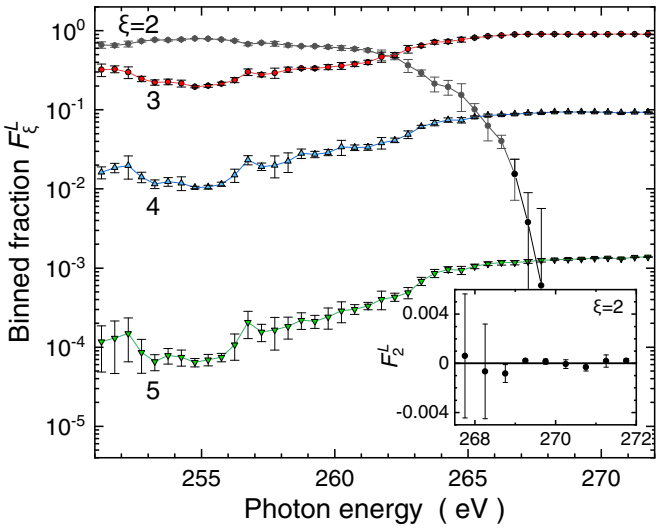

FIG. 8. Charge-state fractions F_ξ^L as functions of the photon energy $E_{\rm ph}$. The inset shows the fraction F_2^L of Ar^{2+} product ions on a linear scale. All error bars are statistical standard deviations. The fractions are shown by different symbols labeled by the final ion charge state ξ. For further details see the main text.

Figure 8 shows charge-state fractions F_ξ^L. The difference in comparison with the fractions F_ξ in Fig. 7 is that here only the effect of L-vacancy production is considered. For this purpose, the new partial cross section $\sigma_{1,2}^L = \sigma_{1,2} - \sigma_{1,2}^M$ was calculated by subtracting the calculated HFR cross section $\sigma_{1,2}^M$ for direct single M-shell ionization from the measured cross section $\sigma_{1,2}$ while the other partial cross sections $\sigma_{1,\xi}^L = \sigma_{1,\xi}$ remained unchanged. The total L-shell absorption cross section is $\sigma_{\rm abs}^L = \sigma_{\rm abs} - \sigma_{1,2}^M$. The symbols with different shadings for different final charge states ξ were obtained by integrating the partial cross sections σ_ξ^L over photon-energy bins of 0.5 eV and calculating the relative fractions F_ξ^L from these numbers. By this procedure, the effects of isolated resonances are averaged out and the statistical uncertainties are reduced.

The fractions F_ξ^L can be interpreted as branching ratios for the decays of argon L-vacancy states. In particular, in the energy range of Fig. 8 only $2p$-hole states can occur either produced by photoexcitation or photoionization of the $2p$ subshell.

Clearly, the decay of an L vacancy depends on the electronic environment. In principle, every excited level has its individual decay probabilities and branching ratios for the emission of electrons and photons. Since measurements are hardly ever level resolved it is difficult to experimentally determine branching ratios for individual levels. In this study we decided to provide branching ratios for photon-energy bins as displayed in Fig. 8. Even with 0.5-eV bins, structure is seen in the branching ratios as a function of photon energy. This is due to the variation of decay probabilities in different groups of resonances. At energies between 250.5 and 252.5 eV the associated L-shell excitation resonances appear to produce slightly higher final charge states than the resonances between 252.5 and 256.5 eV. The resonances around 257 eV favor again higher charge states.

TABLE III. Final charge-state distributions (branching ratios) of argon ions after relaxation of an intermediate $2p$-vacancy state populated via photoabsorption by an initial $Ar^+(3s^2 3p^5)$ ion. The interval 270–271 eV is assumed to provide the fractions that are due to direct ionization of the $2p$ subshell. For this set of charge-state fractions the standard deviations are given both for the present experiment and the measurement by Blancard *et al.* [14]. The associated numbers in parentheses indicate the uncertainties of the last digits of the entries for the charge-state fractions.

$2p^{-1}$ states	Ar^{2+}	Ar^{3+}	Ar^{4+}	Ar^{5+}
Present expt.				
250.5–252.5 eV[a]	0.658	0.321	0.0204	0.000125
252.5–256.5 eV[a]	0.770	0.218	0.0120	0.000074
269.0–272.0 eV[b]	0.0001(4)	0.906(2)	0.093(2)	0.00134(4)
Previous expt. [14]				
≈255 ± 2 eV[a]	0.75	0.24	0.01	
270.0–271.0 eV[b]	0.0(2)	0.91(4)	0.09(2)	
EIMI[c] [60]				
$2p$ ionization	0.0004	0.778	0.222	0
Present theory				
$2p \rightarrow 3d$ res.[a]	0.73	0.26	0.01	
$2p$ ionization	0.0007	0.86	0.13	0.01
Previous theory [61]				
$2p$ ionization	0.0005	0.9995		

[a]$2p$ excitation.
[b]$2p$ ionization.
[c]Electron-impact multiple ionization.

With increasing excitation energy and growing admixtures of direct $2p$ single ionization, the fraction F_2^L dramatically decreases and the charge-state distribution shifts by almost one unit. At energies above ≈269 eV the charge-state fractions level off, staying constant for several eV until effects of double excitations of the Ar^+ parent ion set in at energies above 272 eV. For the energy range 269–272 eV one can assume that essentially only direct $2p$-subshell ionization can take place (on top of direct ionization of the M shell, the contribution of which was subtracted for obtaining the charge-state fractions displayed in Fig. 8). Accordingly, the fractions in that energy window can be solely attributed to the decay of a single $2p$ vacancy in the $Ar^{2+}(2p^{-1}3p^{-1})$ ion.

Table III summarizes these results in wider energy bins and provides comparisons with theoretical results and with other experiments. The comparison of the different results elucidates that it is not straightforward to calculate exact branching ratios for a moderately complex electronic structure. It is all the more reassuring that the present measurement and the previous photoionization experiment [14] provide consistent results for the decay of a $2p$ vacancy in the intermediate $Ar^{2+}(2p^{-1}3p^{-1})$ ion produced by direct ionization of Ar^+. Compared to the previous experiment, the present branching ratios have substantially smaller error bars. The high confidence level of our branching ratios for the decay of intermediate $Ar^{2+}(2p^{-1})$ states is supported by our detailed analysis of the measured partial cross sections $\sigma_{1,\xi}$ in the light

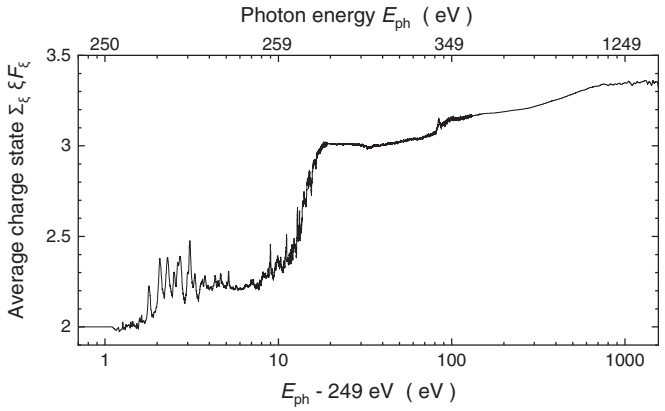

FIG. 9. Argon mean charge state $\bar{\xi}$ as a function of the photon energy. For details see the main text.

of calculations of individual ionization mechanisms (see the following subsections).

At photon energies higher than 272 eV, where the contribution of $\sigma^M_{1,2}$ to the total absorption cross section is becoming negligible and F^L_2 is close to zero, the experimental fractions F_ξ are almost equal to F^L_ξ for $\xi \geqslant 3$ and may therefore also be interpreted as branching ratios associated with L-shell hole-production mechanisms. However, the isolation of specific excitation or ionization processes is complicated. Contributions from direct $2p$ and $2s$ single ionization, double excitations, inner-shell ionization with excitation, and direct double-core-hole production overlap one another so that an intermediate level populated by single-photon absorption cannot be uniquely assigned to any of these processes.

With increasing photon energy E_{ph}, intermediate excited states can be populated that, on average, decay by the emission of an increasing number $m = \xi - 1$ of electrons accompanied by a shift of the charge-state distributions to higher ξ. Consequently, there is an increase of the mean charge state $\bar{\xi} = \sum_\xi \xi F_\xi$ of the Ar ions produced subsequent to the absorption of a photon. Figure 9 displays $\bar{\xi}$ as a function of the photon energy. The average charge state increases, with fluctuations caused by isolated resonances, from $\bar{\xi} = 2$ at 250 eV to $\bar{\xi} = 3.35$ at 1800 eV. The strongest increase is found at the onset of direct single ionization of the $2p$ subshell. The increase of $\bar{\xi}$ at energies beyond approximately 300 eV is partly due to direct $2s$ ionization but can only be explained by the occurrence of multielectron processes both in the population of the intermediate state after photoabsorption and in its subsequent decay. Individual contributions of different photoabsorption product states will be discussed in the following subsections.

C. Cross sections for net multiple photoionization of the Ar^+ ion

In this section, the cross sections $\sigma_{1,m+1}$ for net m-fold ionization ($1 \leqslant m \leqslant 6$) of the Ar^+ ion by a single photon are presented and discussed in the light of theoretical calculations for direct (nonresonant) photo single and double ionization. The cross sections $\sigma_{1,m+1}$ comprise all processes that form $Ar^{(m+1)+}$ ions after the complete relaxation of whichever intermediate state of the argon ion is populated by the absorption of a photon. The theoretical model cross sections $\sigma^d_{1,\xi}$ ($\xi = 2, 3, \ldots, 7$) are each represented by a sum of contributions arising from direct single and double ionization of all subshells that can be reached within the present experimental photon-energy range: $\sigma^d_{1,\xi} = B_\xi(3p)\sigma_{3p} + B_\xi(3s)\sigma_{3s} + B_\xi(2p)\sigma_{2p} + B_\xi(2s)\sigma_{2s} + B_\xi(2p, 3p)\sigma_{2p,3p} + B_\xi(2p, 3s)\sigma_{2p,3s} + B_\xi(2s, 3p)\sigma_{2s,3p} + B_\xi(2s, 3s)\sigma_{2s,3s} + B_\xi(2p, 2p)\sigma_{2p,2p} + B_\xi(2s, 2p)\sigma_{2s,2p} + B_\xi(2s, 2s)\sigma_{2s,2s}$. The quantities $\sigma_{n\ell}$ are the cross sections for direct single ionization of subshell $n\ell$ and $\sigma_{n\ell,n'\ell'}$ stands for direct photo double ionization involving two electrons, one from subshell $n\ell$ and one from $n'\ell'$. The associated quantities $B_\xi(n\ell)$ and $B_\xi(n\ell, n'\ell')$ are the branching ratios for stabilization of the $n\ell$ and $n\ell, n'\ell'$ vacancy states resulting in the population of the $Ar^{\xi+}$ product ions that are observed in the experiments.

By employing the JAC toolbox, a set of branching ratios B_ξ of single- and double-hole states in Ar^+, Ar^{2+}, and Ar^{3+} has been obtained (see Table IV). In the following subsections, the resulting model cross sections $\sigma^d_{1,\xi}$ are compared with the experimental data. As to be expected, the agreement of the model approach and the experimental cross sections is not always perfect. The experimental results have a systematic uncertainty of 15%, the calculated (HFR) cross sections for direct single ionization of a given subshell in argon have an estimated uncertainty of 5%, and a considerably larger uncertainty has to be assigned to the calculation of PDI cross sections. Of course, the calculated branching ratios are also uncertain, mainly because of the limitation of the atomic-state functions to single-configuration state functions (see Sec. III B).

Assuming that the calculated cross sections are correct, an attempt was made to adjust the branching ratios B_ξ such that the model cross sections $\sigma^d_{1,\xi}$ provide a reasonably good representation of the experimental results. The adjusted quantities B_ξ are provided as numbers in parentheses in Table IV. They include the branching ratios $B_\xi(2p)$ found for the decay of a single $2p$ vacancy by scrutinizing the experimental cross sections (see Sec. IV B). While these weight factors $B_\xi(2p)$ can be considered to be accurate, the whole set of B_ξ values is not necessarily unique. However, in combination with the calculated cross sections $\sigma_{n\ell}$ and $\sigma_{n\ell,n'\ell'}$ it results in a remarkably good representation of the measured cross sections $\sigma_{1,\xi}$. Note that $\sum_\xi B_\xi = 1$ (with negligibly small deviations from unity due to rounding effects) for any given vacancy configuration.

1. Net single photoionization

The cross section $\sigma_{1,2}$ for net single ionization of Ar^+ is displayed in Fig. 10. Absolute measurements were carried out and energy-scan data were taken at small photon-energy bandwidths. As discussed in the context of Fig. 6 the experimental energy-scan data can be considered to be taken at a photon-energy resolution of 52 meV.

The normalized scans cover the energy range where $2p$ and $2s$ excitations occur. The peak structure at around 280 eV is due to $2p + 3\ell$ double excitations. The nonresonant part of the cross section is modeled as a sum $\sigma^d_{1,2} = \sigma_{3p} + \sigma_{3s} + 0.0007\sigma_{2p} + 0.000\,09\sigma_{2s}$ of individual contributions, where $\sigma_{n\ell}$ is the cross section for direct single photoionization of subshell $n\ell$. The weight factors resulted from the JAC calculations. The cross sections for direct single ionization of the

TABLE IV. Branching ratios $B_\xi(n\ell)$ and $B_\xi(n\ell, n'\ell')$ for the decay of individual vacancy states contributing to multiple ionization of the Ar^+ ion. These contributions to the production of the final charge states ξ arise from the decay of single- and double-hole configurations that are given at the top of each column. Theoretical branching ratios calculated with JAC are displayed where available. Adjusted B_ξ values are provided by the numbers in parentheses. Missing entries indicate that no branching ratio greater than 10^{-5} was found. The adjusted B_ξ values for a $2p$ vacancy were taken from the detailed analysis described in Sec. IV B.

Product	$2s2s$	$2s2p$	$2p2p$	$2s3s$	$2s3p$	$2p3s$	$2p3p$	$2s$	$2p$	$3s$	$3p$
Ar^{2+}								0.00009	0.0007	1.0	1.0
									(0.0001)	(1.0)	(1.0)
Ar^{3+}				0.0003	0.0003	0.0002	0.002	0.05	0.86		
								(0.20)	(0.906)		
Ar^{4+}	0.00007	0.0006		0.002	0.11	0.86	0.86	0.83	0.13		
					(0.08)	(0.80)	(0.97)	(0.75)	(0.093)		
Ar^{5+}	0.0007	0.36	0.75	1.0	0.89	0.14	0.13	0.12	0.01		
		(0.49)	(0.72)	(0.96)	(0.90)	(0.20)	(0.03)	(0.05)	(0.00134)		
Ar^{6+}	0.24	0.64	0.25								
	(0.29)	(0.50)	(0.28)	(0.04)	(0.02)	(0.002)	(0.0002)				
Ar^{7+}	0.76										
	(0.71)	(0.01)	(0.002)								

different subshells were calculated by employing the HFR theory. A $3p$ and also a $3s$ vacancy in the resulting Ar^{2+} ion can only relax by radiative transitions. Hence, the branching ratio for radiative decay is 1 in both cases.

The resulting model cross section is shown by the short-dashed (violet) line in Fig. 10. It is in very good agreement with the experimental data and can hardly be distinguished from the calculated direct-M-shell-photoionization cross section represented by heavy gray dots in Fig. 10. Using branching ratios from the set of adjusted B_ξ weight factors shown as numbers in parentheses in Table IV produces the (red) solid line. In this case ($\xi = 2$), it is almost indistinguishable from the JAC HFR result. The branching ratio $B_2(2p) = 0.0001(4)$ used in this case for radiative stabilization of a $2p$ vacancy was inferred from the results of the present measurement (see Table III).

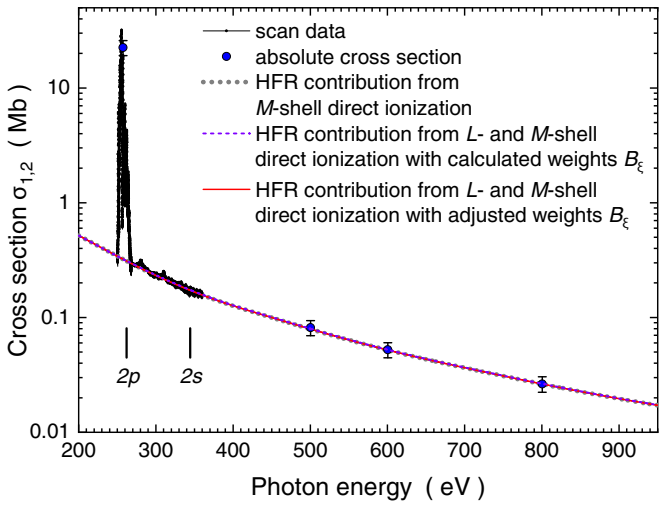

FIG. 10. Net single photoionization cross section $\sigma_{1,2}$ of the Ar^+ ion. Energy-scan data (solid black dots) were taken at a photon-energy resolution of 52 meV in the region of the $2p$ excitation resonances while the energy range 270–360 eV was covered in a scan at ≈170 meV bandwidth. The scan data were normalized to absolute-cross-section measurements (solid blue circles with total error bars). The short-dashed (violet) line is the sum of the HFR results for direct M-shell single ionization (heavy-dotted gray line) and a very small fraction of direct L-shell single ionization with B_ξ values that resulted from the JAC calculations. The solid (red) line is the result obtained with the adjusted set of weight factors B_ξ. Vertical bars indicate the lowest threshold energies for the production of a $2p$ and a $2s$ vacancy by direct ionization, respectively. For more details see the main text.

The comparison of the experimental data with the results of the model calculations represented by the short-dashed (violet) and the solid (red) lines in Fig. 10 shows that direct single ionization of the M shell is the most important Ar^+ single-ionization mechanism over most of the investigated photon-energy range except for the region 250 to 270 eV where $2p$ excitation resonances enhance the cross section by almost two orders of magnitude. Much smaller peak structures arise from $2p + 3\ell$ double- and $2s$ single-excitation resonances. Details of the resonance region are presented and discussed in Sec. IV C 7.

2. Net double photoionization

The cross section $\sigma_{1,3}$ for net double ionization of Ar^+ is displayed in Fig. 11. Absolute measurements were carried out and energy-scan data were taken at different narrow photon-energy bandwidths. However, they are consistent with an overall resolution of 52 meV (see above). The short-dashed (violet) line in Fig. 11 is derived from HFR calculations of σ_{2p} for direct $2p$ and σ_{2s} for direct $2s$ subshell ionization accounting for the JAC branching ratios of decays of the resulting vacancies via single-Auger processes. The resulting model cross section is $\sigma^d_{1,3} = 0.86\sigma_{2p} + 0.05\sigma_{2s} + 0.002\sigma_{2p,3p} + 0.0002\sigma_{2p,3s} + 0.0003\sigma_{2s,3p} + 0.0003\sigma_{2s,3s}$.

The solid (red) line in Fig. 11 is obtained by using the adjusted branching ratios given by the numbers in parentheses in Table IV. The resulting model cross section is $\sigma^d_{1,3} = 0.906\sigma_{2p} + 0.2\sigma_{2s}$. The branching ratio 0.906 for a single-Auger decay of a $2p$ vacancy in the intermediate $Ar^{2+}(2p^{-1}3p^{-1})$ ion results from the present experiment (see

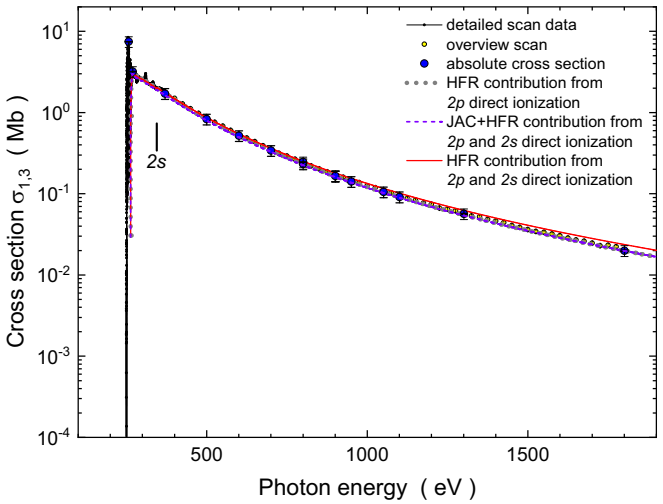

FIG. 11. Net double photoionization cross section $\sigma_{1,3}$ of the Ar^+ ion. Detailed energy-scan data were taken at small bandwidths, all consistent with a 52-meV resolution, in the regions of the $2p$ and $2s$ excitation resonances. The scan data were normalized to absolute-cross-section measurements (solid blue circles with total error bars). The short-dashed (violet) line is the B_ξ-weighted sum of $2s$ and $2p$ HFR results representing the contribution of direct L-shell single ionization. The weight factors B_ξ were obtained by JAC calculations. The solid (red) line is obtained with adjusted branching ratios B_ξ from Table IV. The heavy-dotted gray line is the contribution of $2p$ direct ionization only. The vertical bar indicates the lowest direct-ionization threshold of the $2s$ subshell. The onset of direct $2p$ ionization is obvious from the model cross sections. For more details see the main text.

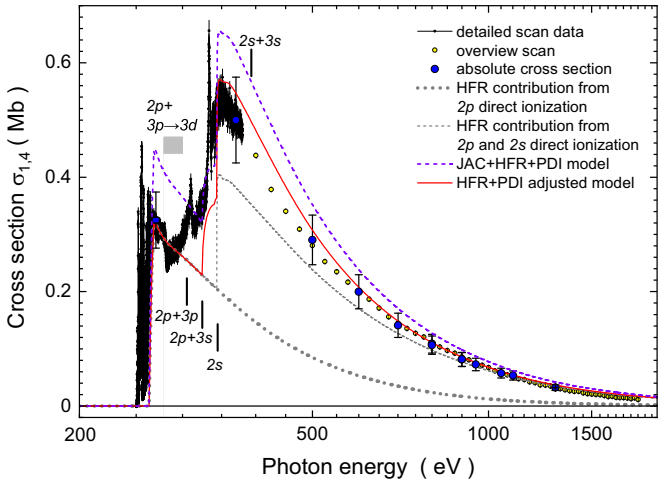

FIG. 12. Net triple photoionization cross section $\sigma_{1,4}$ of the Ar^+ ion. Energy-scan data were taken at different photon-energy bandwidths, all consistent with a 52-meV resolution, covering the regions of the $2p$ and $2s$ excitation resonances and beyond the $2s$ ionization threshold. The scan data were normalized to absolute-cross-section measurements (solid blue circles with total error bars). The short-dashed (violet) line is the model cross section $\sigma^d_{1,4}$ with branching ratios based on the JAC calculations. The solid (red) line is the model cross section with adjusted weight factors B_ξ from Table IV. The heavy-dotted gray line is the contribution of direct $2p$-shell ionization to the solid (red) line, the dashed line additionally includes the contribution of direct $2s$ ionization. The vertical bars indicate the lowest thresholds of direct single and double ionization of various subshells as indicated. The gray-shaded area labeled $2p + 3p \rightarrow 3d$ shows the calculated energy range (see Table II) for direct $2p$ ionization plus $3p \rightarrow 3d$ excitations. For more details see the main text.

Table III). The branching ratio 0.2 for the Auger decay of a $2s$ vacancy was chosen although Kaastra and Mewe [61] and Hahn *et al.* [60] suggested 0.0348 whereas JAC provided $B_2(2s) = 0.05$. The main criterion for the present choice was an overall optimal agreement of the model cross sections with the present experimental results for all product-ion charge states ξ. Apart from that condition, constraints of the values B_ξ result from the condition that the total decay probability of a given vacancy state is 1. Under these constraints, the present choice of $B_\xi(2s) = 0.2$ appears to be adequate although the JAC-based model represents most of the experimental cross section $\sigma_{1,3}$ exceptionally well.

The heavy-dotted line in Fig. 11 is the contribution of $2p$ direct single ionization with the weight factor 0.906 determined in the present experiment as described in Sec. IV B. Obviously, the contribution of direct photoionization of the $2p$ subshell with subsequent single-Auger decay dominates the cross section $\sigma_{1,3}$ by far, except for the energy region of the $2p$ and $2s$ excitation resonances. Excitation is not accounted for in the simple model calculations that are restricted to direct ionization of given subshells. Details of the resonance region are shown and discussed in Sec. IV C 7.

3. Net triple photoionization

The cross section $\sigma_{1,4}$ for net triple ionization of Ar^+ is displayed in Fig. 12. Absolute measurements were carried out and energy-scan data were taken at different narrow photon-energy bandwidths, which are consistent with a 52-meV resolution (see above). The short-dashed (violet) line in Fig. 12 is obtained by employing the JAC branching factors in connection with the HFR and PDI calculations for direct single and double ionization. It represents $\sigma^d_{1,4} = 0.13\sigma_{2p} + 0.83\sigma_{2s} + 0.86\sigma_{2p,3p} + 0.86\sigma_{2p,3s} + 0.11\sigma_{2s,3p} + 0.002\sigma_{2s,3s} + 0.0006\sigma_{2s,2p} + 0.000\,07\sigma_{2s,2s}$. The short-dashed line is somewhat above the experimental cross section $\sigma_{1,4}$, particularly already at energies beyond the $2p$ ionization threshold. This trend continues in the region of the cross-section maximum.

The solid (red) line in Fig. 12 is the model cross section with adjusted weight factors B_ξ as given by the numbers in parentheses in Table IV. It represents $\sigma^d_{1,4} = 0.093\sigma_{2p} + 0.75\sigma_{2s} + 0.97\sigma_{2p,3p} + 0.80\sigma_{2p,3s} + 0.08\sigma_{2s,3p}$. The heavy-dotted line represents the contribution of direct ionization of the $2p$ subshell ($0.093\ \sigma_{2p}$). The dashed line comprises the contribution of the $2s$ subshell ($0.75\ \sigma_{2s}$) in addition. The $2p$ and $2s$ contributions make up for most of the measured cross section $\sigma_{1,4}$. Additional contributions are needed, though, to explain the experimental result. For energies beyond about 305 eV, PDI processes can be assumed to provide the missing cross-section contributions. The late onset of $\sigma_{2p,3p}$ at 319 eV is somewhat artificial since the PDI calculations do not consider the fine-structure splitting in the intermediate $Ar^{3+}(2p^{-1}3p^{-2})$ ion in contrast to the JAC calculation

presented in the second column and the HFR calculation in the fourth column of Table II. In a more realistic PDI calculation, the threshold region should consider the range of level energies associated with the $2p$ and $3p$ vacancies and would thus spread out the onset over a range of approximately 16 eV reaching down to about 305 eV.

Yet, the increase of $\sigma_{1,4}$ starting at about 290 eV remains unexplained by these considerations. Additional contributions to $\sigma_{1,4}$, that have not been calculated and therefore cannot be quantified, might be due to processes involving direct ionization of a core electron and simultaneous excitation of a second electron either from the core or the valence shell. Such ionization-excitation contributions have been considered previously for atoms with a much simpler electronic structure than the present Ar^+ ion. Cross sections for ionization-excitation processes have been calculated for the He-like sequence [62–64] and turned out to be of considerable magnitude.

The apparent onset of an additional triple-ionization channel at about 290 eV in the experimental cross section $\sigma_{1,4}$ may indicate contributions of ionization-excitation processes characterized as $2p, 3p \rightarrow 3d$ (see Table II). Direct ionization of the $2p$ subshell plus excitation $3p \rightarrow 3d$ features the lowest threshold energy of such processes in the present energy range. The configuration $2p^{-1}3p^{-2}3d$ supports a total of 154 levels each of which is reachable from either the $^2P_{3/2}$ ground level of Ar^+ or the first excited level $^2P_{1/2}$. Hence, 308 transitions with their individual cross sections are to be considered to contribute to $\sigma_{1,4}$, just from that configuration alone. The thresholds for reaching these levels span the range indicated by the gray-shaded box in Fig. 12. As Table II shows, the onsets of the associated cross sections span the energy range from about 279 to 300 eV. Excitation to $4s$ instead of $3d$ adds another manifold of possible contributions, and excitations to other subshells $n\ell$ are also possible. The high density of thresholds involved in ionization-excitation processes together with the finite-energy resolution of the experiment and the finite width of the intermediate excited levels can be assumed to produce a relatively smooth cross section as observed in the experiment. We are confident therefore that ionization-excitation contributions are important in the present cross sections for net multiple ionization of the Ar^+ ion. The fact that the magnitude of these contributions is unknown implies substantial difficulties to infer a unique unambiguous set of branching ratios $B_\xi(n\ell, n'\ell')$ (see Table IV) adjusted to the present experiment. Only the branching ratios $B_\xi(2p)$ provided in Tables III and IV can be considered to be of high reliability.

4. Net fourfold photoionization

The cross section $\sigma_{1,5}$ for net fourfold ionization of Ar^+ is displayed in Fig. 13. Absolute measurements were carried out and energy-scan data were taken at different narrow photon-energy bandwidths consistent with a 52-meV resolution (see above). The short-dashed (violet) line in Fig. 13 represents the model cross section $\sigma^d_{1,5} = 0.01\sigma_{2p} + 0.12\sigma_{2s} + 0.13\sigma_{2p,3p} + 0.14\sigma_{2p,3s} + 0.89\sigma_{2s,3p} + 1.0\sigma_{2s,3s} + 0.75\sigma_{2p,2p} + 0.36\sigma_{2s,2p} + 0.0007\sigma_{2s,2s}$ based on the JAC branching ratios B_5. This model cross section greatly

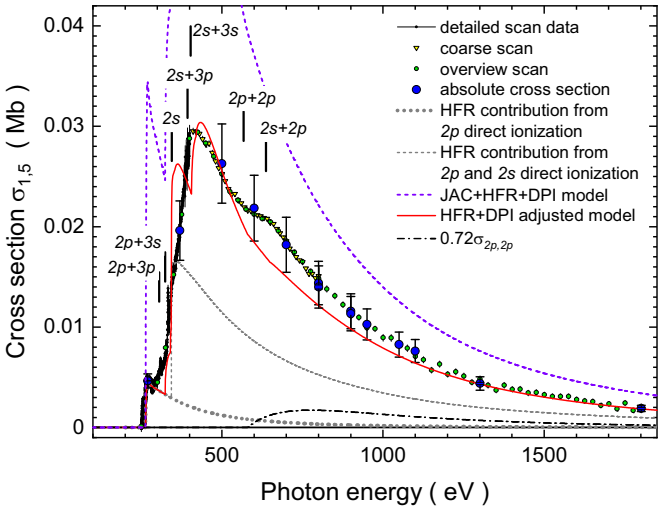

FIG. 13. Net fourfold photoionization cross section $\sigma_{1,5}$ of the Ar^+ ion. Energy-scan data were taken at different photon-energy bandwidths, all consistent with a 52-meV resolution, covering the regions of the $2p$ and $2s$ excitation resonances and beyond the $2s$ ionization threshold. The scan data were normalized to absolute-cross-section measurements (solid blue circles with total error bars). The short-dashed (violet) line is the model cross section $\sigma^d_{1,4}$ with weight factors B_5 obtained by the JAC calculations. The solid (red) line is the model cross section with adjusted weight factors. The heavy-dotted line is the contribution of direct $2p$-shell ionization ($0.00134\sigma_{2p}$), the dashed line additionally includes the contribution of direct $2s$ ionization. The dashed-dotted line represents the contribution of direct double ionization of the $2p$ subshell. The vertical bars indicate the lowest thresholds of direct single and double ionization of various subshells. For more details see the main text.

exceeds the experimental result. In particular, the contribution of direct photoionization of the $2p$ subshell is overestimated (by a factor $\approx$7). The associated weight factor from the JAC calculations is $B_5(2p) = 0.01$ while the analysis of the present measurements (see Sec. IV B and Table III) provided $B_5(2p) = 0.001\,34$. This discrepancy is the main reason for introducing a set of adjusted branching ratios B_ξ for all product-ion charge states ξ. One has to keep in mind in this context that for each vacancy configuration the sum of the associated branching ratios must be unity $\sum_\xi B_\xi = 1$. We also note that charge-state fractions lower than 1% calculated by using the JAC toolbox have an enhanced relative uncertainty which gets amplified in a comparison where the contribution of a percent fraction (in this case of direct $2p$ ionization) makes up for a substantial part of the investigated cross section ($\sigma_{1,5}$ in the present case).

The solid (red) line in Fig. 13 represents $\sigma^d_{1,5} = 0.001\,34\sigma_{2p} + 0.05\sigma_{2s} + 0.03\sigma_{2p,3p} + 0.20\sigma_{2p,3s} + 0.90\sigma_{2s,3p} + 0.96\sigma_{2s,3s} + 0.72\sigma_{2p,2p} + 0.49\sigma_{2s,2p}$ with the adjusted branching ratios B_ξ (the entries in parentheses in Table IV). The heavy-dotted line represents the contribution of direct ionization of the $2p$ subshell ($0.001\,34\ \sigma_{2p}$). The dashed line comprises the contribution of the $2s$ subshell ($0.05\sigma_{2s}$) in addition. At the maximum of $\sigma_{1,5}$, the $2p$ and $2s$ contributions make up for about 50% of the measured cross section. A great deal of the cross section at energies

beyond 400 eV can be rationalized by PDI contributions. The relatively narrow peak feature around 410 eV is interpreted to be mainly due to direct ionization of the $2s$ and 3ℓ subshells. As discussed in connection with Fig. 12, ionization-excitation contributions are likely to occur at energies approximately above 290 eV. Their overlap in photon energy with PDI contributions hinders the determination of branching ratios from the experiment. The peak in the model cross section $\sigma^d_{1,5}$ at about 350 eV is indicative for a possible overestimation of $B_5(2p, 3s)$. The 20% contribution was chosen to reproduce the higher-energy region of $\sigma_{1,5}$ which might also be feasible by introducing realistic ionization-excitation contributions. These, however, are not available.

The bump in the measured cross section $\sigma_{1,5}$ at energies between approximately 550 and 800 eV is not obviously reproduced in the model cross section $\sigma^d_{1,5}$. Its shape follows the calculated PDI cross section $\sigma_{2p,2p}$ for direct double ionization of the $2p$ subshell which is shown as the dashed-dotted line in Fig. 13. Nevertheless, the assumed 72% contribution of $\sigma_{2p,2p}$, although being part of the $\sigma^d_{1,5}$ model function, does not show up as a distinct feature. The reason is the too steeply decreasing model "background" cross section $\sigma^d_{1,5} - 0.72\sigma_{2p,2p}$ which does not include the ionization-excitation processes that probably contribute to the measured cross section $\sigma_{1,5}$.

5. Net fivefold photoionization

The cross section $\sigma_{1,6}$ for net fivefold ionization of Ar^+ is displayed in Fig. 14. Absolute measurements were carried out and energy-scan data were taken at different narrow photon-energy bandwidths, all consistent with a 52-meV resolution. The short-dashed (violet) line in Fig. 14 represents the model cross section $\sigma^d_{1,6} = 0.24\sigma_{2s,2s} + 0.64\sigma_{2s,2p} + 0.25\sigma_{2p,2p}$ obtained by calculating branching ratios B_6 with the JAC toolbox and combining them with HFR and PDI calculations of direct single and double ionizations. The JAC calculations do not predict any sizable contributions of direct $2\ell 3\ell'$ double ionization to the cross section $\sigma_{1,6}$. This may indicate that almost all of the "background" cross section producing signal below ≈600 eV is due to ionization-excitation processes. The solid (red) line represents the model cross section $\sigma^d_{1,6} = 0.0002\sigma_{2p,3p} + 0.002\sigma_{2p,3s} + 0.02\sigma_{2s,3p} + 0.04\sigma_{2s,3s} + 0.28\sigma_{2p,2p} + 0.50\sigma_{2s,2p} + 0.29\sigma_{2s,2s}$ with adjusted weight factors (the entries B_6 in parentheses from Table IV). Single ionization of the L shell with subsequent Auger cascades does not contribute with any significance to the production of such high final charge states. The dashed line shows the contribution of the doubly ionized $2s$ subshell ($0.29\sigma_{2s,2s}$). The dotted line represents the PDI contribution involving a $2s$ and a $2p$ electron ($0.50\sigma_{2s,2p}$) and the dashed-dotted line stands for PDI of the $2p$ subshell ($0.28\sigma_{2p,2p}$). The two contributions resulting from $2p + 2p$ and $2s + 2p$ PDI with subsequent Auger electron emission are approximately equally responsible for most of the measured cross section $\sigma_{1,6}$. The contribution from direct double ionization of the $2s$ subshell is very small. The sum of the latter three contributions is displayed by the dark solid (blue) line in Fig. 14. The cross-section model calculations are in quite good agreement with the experimental results. They

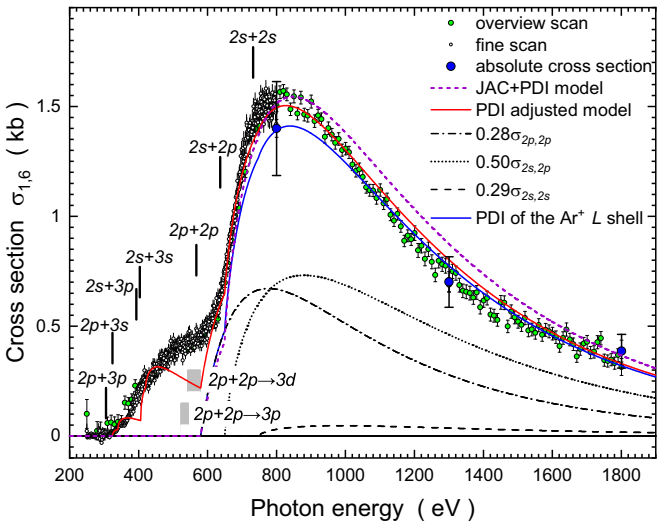

FIG. 14. Net fivefold photoionization cross section $\sigma_{1,6}$ of the Ar^+ ion. Energy-scan data were taken at different photon-energy bandwidths, all consistent with a 52-meV resolution. The scan data were normalized to absolute-cross-section measurements (solid blue circles with total error bars). The short-dashed (violet) line is the model cross section $\sigma^d_{1,6}$ with branching ratios B_6 from the JAC calculations. The lighter solid (red) line is the model cross section with adjusted branching ratios. The darker solid (blue) line is the contribution of PDI of the Ar^+ L shell. The dashed, dotted, and dashed-dotted lines are the PDI contributions arising from $\sigma_{2s,2s}$, $\sigma_{2s,2p}$, and $\sigma_{2p,2p}$, respectively. The vertical bars indicate the lowest thresholds of direct double ionization of various subshells. The gray-shaded areas labeled $2p + 2p \rightarrow 3p$ and $2p + 2p \rightarrow 3d$ show the calculated energy ranges (see Table II) for direct $2p$ ionization plus $2p \rightarrow 3\ell$ excitations. For more details see the main text.

show that $\sigma_{1,6}$ is dominated by PDI producing two vacancies in the L shell.

Different from the result of the JAC calculations, the shoulder in the experimental cross section $\sigma_{1,6}$ at energies below approximately 600 eV can partly be explained by PDI involving one L-shell electron and one M-shell electron. As in the case of $\sigma_{1,4}$, the model calculation $\sigma^d_{1,6}$ does not reproduce the smooth energy dependence of the cross section $\sigma_{1,6}$ between the PDI thresholds. This is particularly obvious in the energy region below 600 eV. In that region, ionization-excitation processes with removal of a $2p$ electron and excitation of a second $2p$ electron to one of the 3ℓ subshells have their thresholds, indicated by the gray shaded areas in Fig. 14. One has to assume that for all PDI pairs $2\ell'$, $3\ell''$ there are infinite series of excitation transitions that may contribute to $\sigma_{1,6}$. However, the result of the PDI calculations for two L-shell electrons represented by the solid (blue) line leaves little space for such "background" cross-section contributions, at least in the energy region beyond 600 eV.

6. Net sixfold photoionization

The cross section $\sigma_{1,7}$ for net sixfold ionization of Ar^+ is displayed in Fig. 15. Absolute measurements were carried out and energy-scan data were taken at different narrow photon-energy bandwidths, all consistent with a 52-meV resolution. The short-dashed (violet) line in Fig. 15 is the model cross

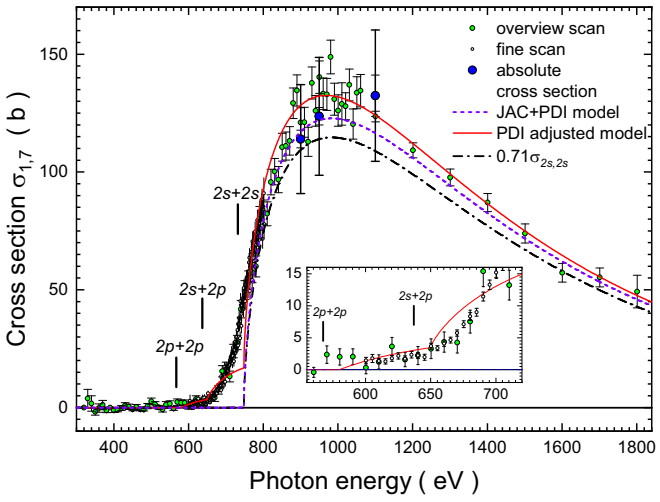

FIG. 15. Net sixfold photoionization cross section $\sigma_{1,7}$ of the Ar^+ ion. Energy-scan data were taken at different photon-energy bandwidths, all consistent with a 52-meV resolution. The scan data were normalized to absolute-cross-section measurements (solid blue circles with total error bars). The short-dashed (violet) line is the model cross section $\sigma^d_{1,6} = 0.76\sigma_{2s,2s}$ using the JAC weight factor $B_7(2s, 2s)$ from Table IV. The solid (red) line is the model cross section with adjusted weight factors B_7. The dashed-dotted line is the contribution of PDI of the $2s$ subshell with the adjusted $B_7(2s, 2s) = 0.71$. The inset shows a blowup of the double-L-shell ionization threshold region. The solid data points were generated from the fine-scan data (small open circles in the main figure) by averaging over 5-eV bins. The vertical bars indicate the lowest thresholds of direct double ionization of various subshells as indicated. For more details see the main text.

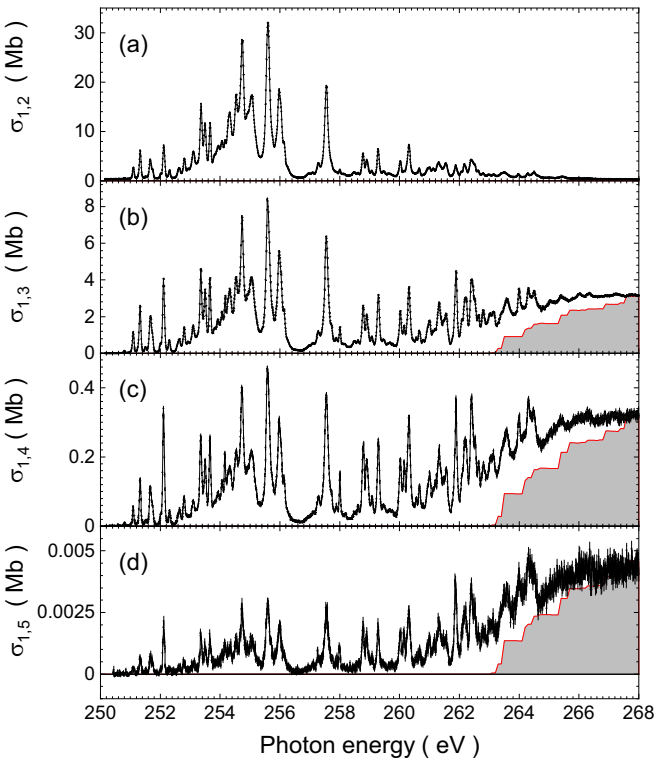

FIG. 16. Experimental cross sections for Ar^+ in the photon-energy range of the $2p$ excitation resonances: net single ionization (a), net double ionization (b), net triple ionization (c), and net quadruple ionization (d). All spectra were measured at a photon-energy resolution of 52 meV. The solid (red) lines with light gray shading represent the contributions of direct ionization of the $2p$ subshell calculated on the basis of the HFR theory. The calculated absorption cross sections were multiplied with the branching ratios provided in Table III for "$2p$ ionization."

section $\sigma^d_{1,7} = 0.76\sigma_{2s,2s}$ with the weight factor $B_7(2s, 2s) = 0.76$ from the JAC calculation. It is in quite good agreement with the experiment at photon energies beyond approximately 800 eV but does not reproduce the cross section at energies below ≈730 eV. The solid (red) line represents the model cross section $\sigma^d_{1,7} = 0.002\sigma_{2p,2p} + 0.01\sigma_{2s,2p} + 0.71\sigma_{2s,2s}$. The adjusted weight factors of the direct double-ionization cross sections are the branching ratios in parentheses from Table IV. The dashed-dotted line shows the contribution of the doubly ionized $2s$ subshell ($0.71\sigma_{2s,2s}$). The contribution arising from direct double ionization of the $2s$ subshell is responsible for almost all of the measured cross section $\sigma_{1,7}$. The contributions from direct double ionization involving two $2p$ electrons or one from the $2s$ and one from the $2p$ subshell are both small.

The inset of Fig. 15 highlights the sensitivity of the present experiment. The cross sections between 600 and 645 eV are only 1.8 b on average with total uncertainties of less than 0.4 b. The vertical bars show the lowest threshold energies (see Table II) calculated for the production of two holes in the $2p$ subshell ($2p + 2p$) and one hole in the $2s$ and another in the $2p$ subshell ($2s + 2p$). The solid (red) line represents the PDI model with cross sections calculated for the configuration average rather than individual double-core-vacancy levels. Considering the difference between the lowest threshold and the configuration-averaged double-ionization onset the experimental data obviously show the opening of the $2p + 2p$ and the $2s + 2p$ double-ionization channels. The associated measured cross sections are only a few b and hence their measurement required the unprecedentedly high sensitivity of this photon-ion merged-beams experiment.

7. Resonance contributions

This section highlights the regions where pronounced resonances occur in m-fold ionization. In particular, resonant excitation of the $2p$ and the $2s$ subshells are expected in the energy ranges 250–270 eV and approximately 300–350 eV, respectively. In addition, contributions of double excitations at energies beyond 270 eV were to be expected. In the energy region of interest (270 to 300 eV), such double excitations involve one electron from the $2p$ subshell and one additional electron from either the $3s$ or the $3p$ subshells.

Figure 16 displays the measured spectra for net single, double, triple, and quadruple photoionization of Ar^+ in the energy region where a $2p$ electron can be excited to the $3d$ subshell or to the ns or nd subshells with $n = 4, 5, 6, \ldots$. The intermediate excited states, all with a vacancy in the $2p$ subshell, can decay by cascades of Auger decays. The experiment shows that up to four electrons can be ejected from $Ar^+(2p^{-1})$ core-hole levels. The branching ratios for these decays differ from one another by large factors as discussed already in

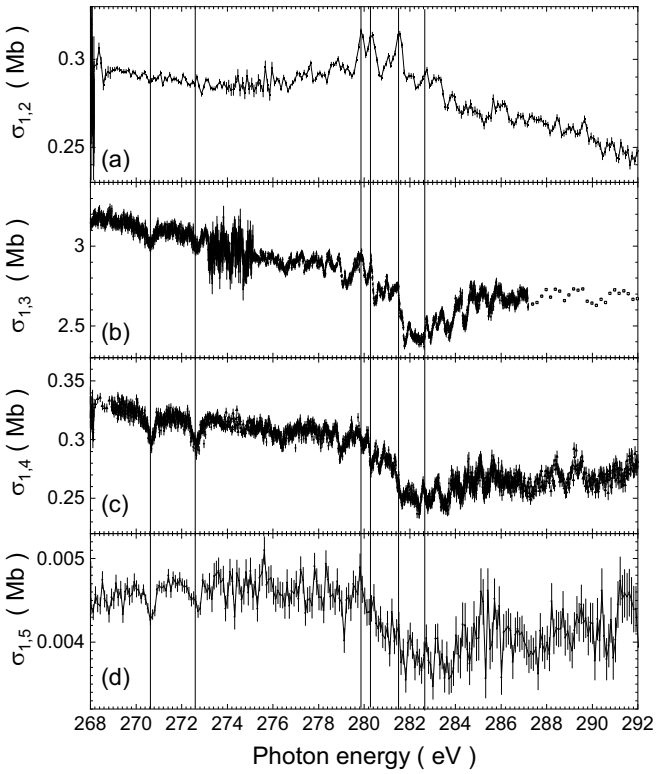

FIG. 17. Experimental cross sections for Ar^+ in the photon-energy range of the $2p + 3\ell$ double-excitation resonances: net single ionization (a), net double ionization (b), net triple ionization (c), and net quadruple ionization (d). The spectra in different energy regions were measured at different photon-energy resolutions ranging from 52 meV to at most 400 meV. Vertical lines indicate positions of resonances.

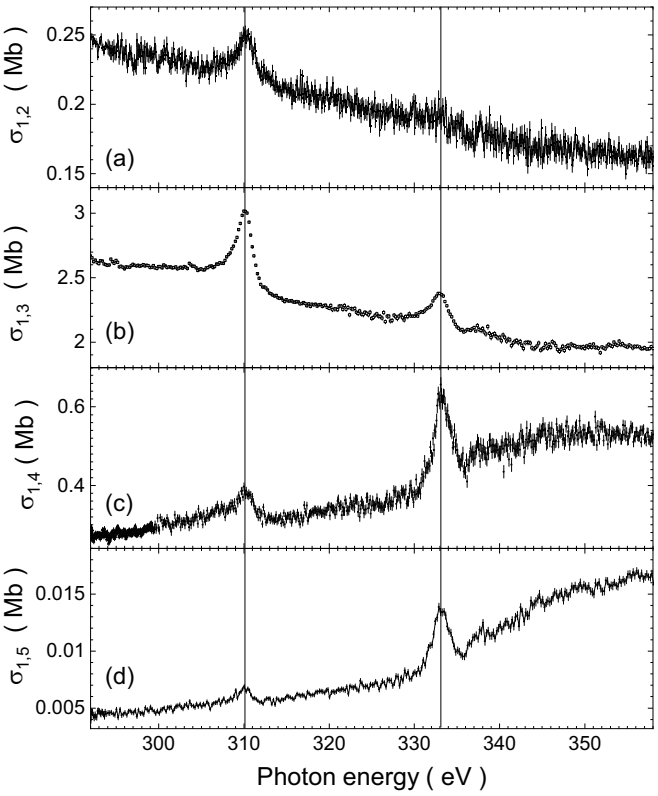

FIG. 18. Experimental cross sections for Ar^+ in the photon-energy range of the $2s$ excitation resonances: net single ionization (a), net double ionization (b), net triple ionization (c), and net quadruple ionization (d). Vertical lines indicate the positions of the $2s \rightarrow 3p$ and $2s \rightarrow 4p$ resonances.

Sec. IV. Cross sections for net single photoionization at an energy resolution of 52 meV reach up to about 30 Mb, for net double photoionization they are down to approximately 8 Mb at their maximum, for net triple photoionization they do not quite reach the maximum of 0.5 Mb, and quadruple ionization resonances are generally smaller than about 4 kb. No measurable signal could be found for net quintuple ionization in the energy range below 270 eV. We also note that the probabilities for multiphoton absorption are too small to produce measurable signals. This aspect of experiments at the PIPE setup has been discussed in detail previously [65,66].

Figure 16 also displays model cross sections for the production of $Ar^{\xi+}$ ions from Ar^+ on the basis of HFR cross sections for direct $2p$ single photoionization multiplied with experimentally derived branching ratios from Table III. There are a number of individual thresholds for direct $2p$ photoionization associated with specific $Ar^{2+}(2p^{-1})$ core-hole levels.

Figure 17 shows the measured spectra for net single, double, triple, and quadruple photoionization of Ar^+ in the energy region 268–292 eV where a $2p$ electron and, simultaneously, a $3s$ or a $3p$ electron can be excited. Although such double excitations had to be expected, it is surprising to see how strongly they affect the different photoionization cross sections. The natural widths of the resonance features in the investigated energy range are apparently greater than 400 meV: Convolutions of the calculated HFR cross section with Gaussians of 52 to 170 meV FWHM do not show significant differences in the resulting convoluted spectra (confer Fig. 6).

While double-excitation resonances in the channel of net single photoionization add to the size of the cross section, most resonance features seen in net double, triple, or quadruple ionization are window resonances. That is, the associated amplitudes of resonant excitation and direct ionization destructively interfere with one another and, thus, dips in the cross section are observed. These are particularly strong at energies around 280 eV. In the single-ionization channel there is hardly any contribution from direct $2p$ ionization with subsequent Auger decays present and, hence, there is no partner channel for resonances to interfere with. Therefore, the double-excitation resonances show no obvious sign of interference and just add to the observed single-ionization cross section.

Figure 18 displays the measured spectra for net single, double, triple, and quadruple photoionization of Ar^+ in the energy region 290–360 eV where a $2s$ electron can be excited to a np subshell with $n = 3, 4, 5, \ldots$. The intermediate excited states, all with a vacancy in the $2s$ subshell, can decay by cascades of Auger decays. Ejection of up to four electrons from $Ar^+(2s^{-1})$ core-hole levels has been observed. The $2s$-excitation resonances are quite broad. The large widths of more than 2 eV are caused by the opening of

TABLE V. Final charge-state distributions (branching ratios) of argon ions after relaxation of an intermediate $2s$-vacancy state populated via $2s$ photoexcitation of an initial $Ar^+(3s^2 3p^5)$ ion. The numbers in parentheses behind the entries for branching ratios show the uncertainties of the last one or two digits. The present results may also be compared with branching ratios obtained from direct ionization of the $2s$ subshell in neutral argon populating the identical intermediate $Ar^+(2s^{-1})$ configuration.

Excitation	Ar^{2+}	Ar^{3+}	Ar^{4+}	Ar^{5+}
This expt.				
$2s \rightarrow 3p$	0.034(2)	0.87(3)	0.091(4)	0.00084(9)
$2s \rightarrow 4p$	0.020(9)	0.57(3)	0.40(2)	0.0088(9)
This theory				
$2s \rightarrow 3p$	0.06	0.85	0.09	0
$2s \rightarrow 4p$	0.05	0.95	0	0
Ar $2s \rightarrow \infty$				
Expt. [26]	0.01(4)	0.89(3)	0.10(2)	-
Expt. [27]	0.03	0.89	0.08	0.003
Theory [61]	0.0361	0.9634	0	0
Theory [67]	0.042	0.934	0.025	0
Theory [27]	0.05	0.95	0	0
Theory [68]	0.035	0.887	0.075	0.0026

Coster-Kronig decay channels when a $2s$ vacancy is formed. Again, measurements were carried out at different photon-energy bandwidths between 52 and 400 meV. The $2s$ resonance features are much broader than the experimental bandwidths so that the $2s$ resonances were essentially observed with their natural widths.

The branching ratios for the decays of $2s$ vacancy levels in Ar^+ produced by excitations $2s \rightarrow 3p, 4p$ into different final channels, characterized by the final charge state of the argon ion, substantially differ from one another. In order to assess these branching ratios, the peak areas of the $2s \rightarrow 3p$ excitation resonances at about 310 eV and of the $2s \rightarrow 4p$ resonances at about 333 eV were determined and the branching ratios inferred. Uncertainties of the peak areas arise from statistical uncertainties and from difficulties with isolating the $2s$ resonances from all the other cross-section contributions (the "background"). The experimentally inferred branching ratios are shown in Table V. The results of the present JAC calculations for the $2s \rightarrow 3p$ and $2s \rightarrow 4p$ resonances are also provided in this table. While the branching ratios for the $2s \rightarrow 3p$ excitation resonance are in fairly good agreement with the experiment, the JAC calculations for the $2s \rightarrow 4p$ resonance underestimate the probability to produce Ar^{4+} by Auger decays subsequent to the initial photoexcitation process. In particular, the experimental spectra show a strong shift of the relative importance of the $2s$ resonances from $2s \rightarrow 3p$ dominating in the single ionization of Ar^+ to $2s \rightarrow 4p$ dominating in triple and quadruple ionization of Ar^+. This trend is not reproduced by the calculations. This may be attributed to the fact that the cascade processes are considerably more complex for the intermediate $Ar^+(2s^{-1}3p^{-1}4p)$ ion with three open shells produced by $2s \rightarrow 4p$ excitation compared to $Ar^+(2s^{-1})$ with only a single electron in the open $2s$ shell produced by $2s \rightarrow 3p$ excitation.

The intermediate $Ar^+(2s^{-1})$ configuration observed in the present experiments through its resonant $2s \rightarrow 3p$ contributions to the measured cross sections $\sigma_{1,\xi}$ of the Ar^+ ion is identical to the configuration produced by direct $2s$ ionization of the neutral Ar atom. In previous experiments [26,27] the decay of this $2s$-hole configuration has been investigated by coincident Auger-electron spectroscopy. From these measurements the final charge-state fractions of argon ions produced by Auger decays of the $Ar^+(2s^{-1})$ configuration were inferred. The results are also shown in Table V. Previous theoretical treatments [27,61,67] of this problem provided results that are also included in Table V. A very recent comprehensive calculation by Liu *et al.* [68] is in remarkably good agreement with the charge-state fractions experimentally inferred by Lablanquie *et al.* [27]. A comparison of the data obtained from Auger spectroscopy measurements [26,27] with the results of the present experiment shows good agreement for the lower final charge states $Ar^{\xi+}$ up to $\xi = 4$. However, for the production of Ar^{5+} ions the present probability is about one third of the previous results obtained by Lablanquie *et al.* [27] and Liu *et al.* [68]. Brünken *et al.* [26] could not find evidence for the production of Ar^{5+} at all.

The observation of the $2s \rightarrow 3p$ resonance contribution to the measured cross section $\sigma_{1,5}$ (see Fig. 18) is an unambiguous signature of Auger decays releasing four electrons from the intermediate $Ar^+(2s^{-1})$ ion. The uncertainty of the peak area relative to the $2s \rightarrow 3p$ resonances in the cross sections $\sigma_{1,\xi}$ with $\xi = 2, 3, 4$ is only about 10% and thus cannot explain the observed differences.

V. SUMMARY AND OUTLOOK

Absolute cross sections for single and multiple photoionization of Ar^+ ions have been measured in the energy range 250 to 1800 eV. All accessible final channels from Ar^{2+} to Ar^{7+} were investigated in great detail. A large range of cross-section magnitudes from 1 b to 30 Mb could be covered. The smallest cross section that could be measured with an acceptable uncertainty was approximately 2 ± 1 b.

Detailed energy scans were performed at photon-energy bandwidths corresponding to an effective resolution of 52 meV. These measurements showed distinct $2p \rightarrow n\ell$ excitation resonances in the photon-energy range 250–270 eV, numerous $2p, 3\ell \rightarrow 3\ell', n\ell''$ double-excitation features in the photon-energy range 270–300 eV, and few $2s \rightarrow np$ resonance peaks at photon energies up to about 350 eV. Total photoabsorption cross sections of the Ar^+ ion in the photon energy range 250–1800 eV were inferred from the experimental data. Comparison of these results with Hartree-Fock calculations including relativistic corrections shows good agreement.

The partial experimental cross sections $\sigma_{1,\xi}$ for the production of $Ar^{\xi+}$ ($\xi = 2, 3, \ldots, 7$) from Ar^+ could be employed to determine the average charge of the product ions after absorption of a photon by an Ar^+ ion. Branching ratios for the production of different final ion charge states by cascades of decay processes could be experimentally determined for a number of hole states produced in the photoabsorption by the Ar^+ ion. Particularly reliable results were obtained for the decay of a $2p$ vacancy in $Ar^{2+}(2s^2 2p^5 3s^2 3p^5)$.

A self-consistent set of product-ion charge-state distributions was calculated for $2s$ and $2p$ single core-hole and $2s+2s$, $2s+2p$, $2p+2p$, $2s+3s$, $2s+3p$, $2p+3s$, $2p+3p$ double-vacancy configurations including at least one L-shell core hole. All these configurations are relevant to photoabsorption by Ar^+ in the present photon-energy range. In addition, the cross sections for producing all these single- and double-hole states were calculated using different theoretical models. The results are in very favorable accord with the experimental cross sections. In particular, it is shown that direct photo double ionization starts to play a role in the production of Ar^{4+}, double-L-shell ionization is responsible for most of the cross section $\sigma_{1,6}$, while $\sigma_{1,7}$ is almost exclusively determined by the process of direct photo double ionization of the $2s$ subshell and subsequent emission of four electrons.

For fully explaining the observed cross sections $\sigma_{1,\xi}$ with $\xi = 4, 5, 6, 7$ it is necessary to consider higher-order processes such as ionization with excitation and direct photo double ionization. Given the relative complexity of the Ar^+ ion, ionization-excitation calculations were not attempted in this study. Nevertheless, the overall agreement of a combination of several theoretical contributions, including calculations of cross sections for direct single and double ionization as well as extensive computations of associated decay cascades, with experimental cross sections measured on an absolute scale is remarkable.

Important improvement of the theoretical calculations both of direct double ionization and of decay cascades may be expected when the different theoretical approaches are extended by considering the contributions of individual levels rather than configuration averages. Moreover, cascade calculations should include Auger processes involving more than two electrons. It would also be desirable to tackle the problem of ionization-excitation contributions to multiple ionization induced by photoabsorption. All these improvements and extensions will greatly enhance the complexity of the theoretical calculations, however, their implementation is not impossible. On the experimental side, it would be highly desirable to include the observation of emitted electrons. This is particularly difficult given the low-particle density of a typical ion beam. Nevertheless, earlier attempts to register electron emission in photon-ion interaction experiments have been successful in a few special cases. Higher densities in the primary-ion beam can probably be achieved by employing specialized ion sources. By switching to ions with a smaller number of electrons some of the complexity and difficulties can be removed. As a result, one may expect a better quantitative understanding of, e.g., direct photo double ionization processes.

ACKNOWLEDGMENTS

This research was carried out in part at the light source PETRA III at DESY, a member of the Helmholtz Association (HGF). We would like to thank K. Bagschik, J. Buck, F. Scholz, J. Seltmann, and M. Hoesch for their help with using beamline P04. We thank Dr. J.-M. Bizau for providing us with the numerical data obtained in the Ar^+ cross-section measurements at SOLEIL. We acknowledge the contribution to this project by the late Dr. S. Ricz, Debrecen, Hungary, both in the design and construction of the PIPE setup and in the Ar^+ experiments. We are grateful for support from Bundesministerium für Bildung und Forschung within the 'Verbundforschung' funding scheme (Grants No. 05K16GUC, No. 05K16RG1, No. 05K16SJA1, No. 05K19GU3, and No. 05K19RG3) and from Deutsche Forschungsgemeinschaft (DFG, German Research Foundation - Projects No. 245652604, No. 389115454, and No. 201267377).

[1] K. Ueda, E. Sokell, S. Schippers, F. Aumayr, H. Sadeghpour, J. Burgdörfer, C. Lemell, X.-M. Tong, T. Pfeifer, F. Calegari, A. Palacios, F. Martin, P. Corkum, G. Sansone, E. V. Gryzlova, A. N. Grum-Grzhimailo, M. N. Piancastelli, P. M. Weber, T. Steinle, K. Amini *et al.*, Roadmap on photonic, electronic and atomic collision physics: I. Light-matter interaction, J. Phys. B: At., Mol. Opt. Phys. **52**, 171001 (2019).

[2] A. Müller, Precision studies of deep-inner-shell photoabsorption by atomic ions, Phys. Scr. **90**, 054004 (2015).

[3] S. Schippers, A. L. D. Kilcoyne, R. A. Phaneuf, and A. Müller, Photoionisation of ions with synchrotron radiation: From ions in space to atoms in cages, Contemp. Phys. **57**, 215 (2016).

[4] T. Andersen, Atomic negative ions: Structure, dynamics and collisions, Phys. Rep. **394**, 157 (2004).

[5] D. J. Pegg, Structure and dynamics of negative ions, Rep. Prog. Phys. **67**, 857 (2004).

[6] J. B. West, Photoionization of atomic ions, J. Phys. B: At., Mol. Opt. Phys. **34**, R45 (2001).

[7] I. C. Lyon, B. Peart, J. B. West, and K. Dolder, Measurements of absolute cross sections for the photoionisation of Ba^+ ions, J. Phys. B: At., Mol. Opt. Phys. **19**, 4137 (1986).

[8] H. Kjeldsen, Photoionization cross sections of atomic ions from merged-beam experiments, J. Phys. B: At., Mol. Opt. Phys. **39**, R325 (2006).

[9] S. Schippers, T. Buhr, A. Borovik Jr., K. Holste, A. Perry-Sassmannshausen, K. Mertens, S. Reinwardt, M. Martins, S. Klumpp, K. Schubert, S. Bari, R. Beerwerth, S. Fritzsche, S. Ricz, J. Hellhund, and A. Müller, The photon-ion merged-beams experiment PIPE at PETRA III - The first five years, X-Ray Spectrom. **49**, 11 (2020).

[10] S. Schippers and A. Müller, Photoionization of astrophysically relevant atomic ions at PIPE, Atoms **8**, 45 (2020).

[11] R. C. Bilodeau, N. D. Gibson, J. D. Bozek, C. W. Walter, G. D. Ackerman, P. Andersson, J. G. Heredia, M. Perri, and N. Berrah, High-charge-state formation following inner-shell photodetachment from S^-, Phys. Rev. A **72**, 050701(R) (2005).

[12] S. Schippers, A. Perry-Sassmannshausen, T. Buhr, M. Martins, S. Fritzsche, and A. Müller, Multiple photodetachment of atomic anions via single and double core-hole creation, J. Phys. B: At., Mol. Opt. Phys. **53**, 192001 (2020).

[13] M. Habibi, D. A. Esteves, R. A. Phaneuf, A. L. D. Kilcoyne, A. Aguilar, and C. Cisneros, Photoionization cross sections

for ions of the cerium isonuclear sequence, Phys. Rev. A **80**, 033407 (2009).

[14] C. Blancard, Ph. Cossé, G. Faussurier, J.-M. Bizau, D. Cubaynes, N. El Hassan, S. Guilbaud, M. M. Al Shorman, E. Robert, X.-J. Liu, C. Nicolas, and C. Miron, *L*-shell photoionization of Ar^+ to Ar^{3+} ions, Phys. Rev. A **85**, 043408 (2012).

[15] S. Schippers, R. Beerwerth, S. Bari, T. Buhr, K. Holste, A. L. D. Kilcoyne, A. Perry-Sassmannshausen, R. A. Phaneuf, S. Reinwardt, D. W. Savin, K. Schubert, S. Fritzsche, M. Martins, and A. Müller, Near *L*-edge single and multiple photoionization of doubly charged iron ions, Astrophys. J. **908**, 52 (2021).

[16] A. M. Covington, A. Aguilar, I. R. Covington, G. Hinojosa, C. A. Shirley, R. A. Phaneuf, I. Álvarez, C. Cisneros, I. Dominguez-Lopez, M. M. Sant'Anna, A. S. Schlachter, C. P. Ballance, and B. M. McLaughlin, Valence-shell photoionization of chlorinelike Ar^+ ions, Phys. Rev. A **84**, 013413 (2011).

[17] A. Müller and R. Frodl, *L*-Shell Contributions to Multiple Ionization of Ar^{i+} Ions ($i = 1, 2, 3$) by Electron Impact, Phys. Rev. Lett. **44**, 29 (1980).

[18] A. Müller, E. Salzborn, R. Frodl, R. Becker, H. Klein, and H. Winter, Absolute ionisation cross sections for electrons incident on O^+, Ne^+, Xe^+ and Ar^{i+}(i=1,...,5) ions, J. Phys. B: At., Mol. Opt. Phys. **13**, 1877 (1980).

[19] A. Müller, K. Huber, K. Tinschert, R. Becker, and E. Salzborn, An improved crossed-beams technique for the measurement of absolute cross sections for electron impact ionisations of ions and its application to Ar^+ ions, J. Phys. B: At., Mol. Opt. Phys. **18**, 2993 (1985).

[20] A. Müller, K. Tinschert, C. Achenbach, R. Becker, and E. Salzborn, Electron impact double ionisation of Ar^+ and Ar^{4+} ions, J. Phys. B: At., Mol. Opt. Phys. **18**, 3011 (1985).

[21] K. Tinschert, A. Müller, R. A. Phaneuf, G. Hofmann, and E. Salzborn, Electron impact double ionisation of Ar^{q+} ions (q=1, 2,..., 7): Two-electron processes compared with inner-shell contributions, J. Phys. B: At., Mol. Opt. Phys. **22**, 1241 (1989).

[22] D. S. Belic, J. Lecointre, and P. Defrance, Electron impact multiple ionization of argon ions, J. Phys. B: At., Mol. Opt. Phys. **43**, 185203 (2010).

[23] A. Müller, A. L. D. Kilcoyne, R. A. Phaneuf, K. Holste, S. Schippers, and A. S. Kheifets, Direct double ionization of the Ar^+M shell by a single photon, Phys. Rev. A **103**, L031101 (2021).

[24] N. B. Tyndall, C. A. Ramsbottom, C. P. Ballance, and A. Hibbert, Valence and L-shell photoionization of Cl-like argon using R-matrix techniques, Mon. Not. R. Astron. Soc. **456**, 366 (2016).

[25] N. Saito and I. H. Suzuki, Multiple photoionization in Ne, Ar, Kr and Xe from 44 to 1300 eV, Int. J. Mass Spectrom. Ion Processes **115**, 157 (1992).

[26] S. Brünken, Ch. Gerth, B. Kanngießer, T. Luhmann, M. Richter, and P. Zimmermann, Decay of the Ar $2s^{-1}$ and $2p^{-1}$ and Kr $3p^{-1}$ and $3d^{-1}$ hole states studied by photoelectron-ion coincidence spectroscopy, Phys. Rev. A **65**, 042708 (2002).

[27] P. Lablanquie, S.-M. Huttula, M. Huttula, L. Andric, J. Palaudoux, J. H. D. Eland, Y. Hikosaka, E. Shigemasa, K. Ito, and F. Penent, Multi-electron spectroscopy: Auger decays of the argon 2*s* hole, Phys. Chem. Chem. Phys. **13**, 18355 (2011).

[28] X. L. Wang, B. X. Liu, G. H. Zhang, P. Y. Wang, L. W. Liu, and X. Y. Li, Theoretical studies on the cascade decay processes of 1s-core-hole state of Ar ion, J. Electron. Spectrosc. Relat. Phenom. **250**, 147083 (2021).

[29] S. Schippers, S. Ricz, T. Buhr, A. Borovik Jr., J. Hellhund, K. Holste, K. Huber, H.-J. Schäfer, D. Schury, S. Klumpp, K. Mertens, M. Martins, R. Flesch, G. Ulrich, E. Rühl, T. Jahnke, J. Lower, D. Metz, L. P. H. Schmidt, M. Schöffler *et al.*, Absolute cross sections for photoionization of Xe^{q+} ions ($1 \leqslant q \leqslant 5$) at the 3d ionization threshold, J. Phys. B: At., Mol. Opt. Phys. **47**, 115602 (2014).

[30] A. Müller, D. Bernhardt, A. Borovik Jr., T. Buhr, J. Hellhund, K. Holste, A. L. D. Kilcoyne, S. Klumpp, M. Martins, S. Ricz, J. Seltmann, J. Viefhaus, and S. Schippers, Photoionization of Ne atoms and Ne^+ ions near the K edge: Precision spectroscopy and absolute cross-sections, Astrophys. J. **836**, 166 (2017).

[31] J. Viefhaus, F. Scholz, S. Deinert, L. Glaser, M. Ilchen, J. Seltmann, P. Walter, and F. Siewert, The variable polarization XUV beamline P04 at PETRA III: Optics, mechanics and their performance, Nucl. Instrum. Methods Phys. Res., Sect. A **710**, 151 (2013).

[32] R. A. Phaneuf, C. C. Havener, G. H. Dunn, and A. Müller, Merged-beams experiments in atomic and molecular physics, Rep. Prog. Phys. **62**, 1143 (1999).

[33] J. Fricke, A. Müller, and E. Salzborn, Single particle counting of heavy ions with a channeltron detector, Nucl. Instrum. Methods **175**, 379 (1980).

[34] K. Rinn, A. Müller, H. Eichenauer, and E. Salzborn, Development of single-particle detectors for keV ions, Rev. Sci. Instrum. **53**, 829 (1982).

[35] J. Buck, K. Bagschik, L. Glaser, F. Scholz, J. Seltmann, and J. Viefhaus, Progress report on the XUV online diagnostic unit for the highly accurate determination of SR properties, in *Proceedings of the 13th International Conference on Synchrotron Radiation Instrumentation SRI2018*, AIP Conf. Proc. No. 2054 (AIP, Melville, NY, 2019), p. 060057.

[36] G. C. King, M. Tronc, F. H. Read, and R. C. Bradford, An investigation of the structure near the $L_{2,3}$ edges of argon, the $M_{4,5}$ edges of krypton and the $N_{4,5}$ edges of xenon, using electron impact with high resolution, J. Phys. B: At., Mol. Opt. Phys. **10**, 2479 (1977).

[37] M. Tronc, G. C. King, and F. H. Read, Carbon K-shell excitation in small molecules by high-resolution electron impact, J. Phys. B: At., Mol. Opt. Phys. **12**, 137 (1979).

[38] R. N. S. Sodhi and C. E. Brion, Reference energies for inner shell electron energy-loss spectroscopy, J. Electron Spectrosc. Relat. Phenom. **34**, 363 (1984).

[39] F. Wuilleumier, Excitations simples et multiples dans les couches atomiques internes des gaz rares sous l'action des rayons x, J. Phys. Colloques **32**, C4-88 (1971).

[40] A. Müller, E. Lindroth, S. Bari, A. Borovik, Jr., P.-M. Hillenbrand, K. Holste, P. Indelicato, A. L. D. Kilcoyne, S. Klumpp, M. Martins, J. Viefhaus, P. Wilhelm, and S. Schippers, Photoionization of metastable heliumlike $C^{4+}(1s2s\ ^3S_1)$ ions: Precision study of intermediate doubly excited states, Phys. Rev. A **98**, 033416 (2018).

[41] R. D. Cowan, *The Theory of Atomic Structure and Spectra* (University of California Press, Berkeley, 1981).

[42] M. Martins, Photoionization of open-shell atoms: The chlorine 2p excitation, J. Phys. B: At., Mol. Opt. Phys. **34**, 1321 (2001).

[43] S. Fritzsche, A fresh computational approach to atomic structures, processes and cascades, Comput. Phys. Commun. **240**, 1 (2019).

[44] I. P. Grant, *Relativistic Quantum Theory of Atoms and Molecules: Theory and Computation*, Springer Series on Atomic, Optical, and Plasma Physics (Springer, New York, 2007).

[45] S. Fritzsche, Large-scale accurate structure calculations for open-shell atoms and ions, Phys. Scr. **T100**, 37 (2002).

[46] J. Bezanson, J. Chen, B. Chung, S. Karpinski, V. B. Shah, J. Vitek, and J. Zoubritzky, Julia: Dynamism and performance reconciled by design, Proc. ACM Program. Lang. **2**, 120 (2018).

[47] S. Fritzsche, P. Palmeri, and S. Schippers, Atomic cascade computations, Symmetry **13**, 520 (2021).

[48] S. Fritzsche, B. Fricke, and W.-D. Sepp, Reduced L_1 level width and Coster-Kronig yields by relaxation and continuum interactions in atomic zinc, Phys. Rev. A **45**, 1465 (1992).

[49] S. Fritzsche, JAC: User Guide, Compendium & Theoretical Background, available from https://github.com/OpenJAC/JAC.jl.

[50] J. H. McGuire, *Electron Correlation Dynamics in Atomic Collisions* (Cambridge University Press, Cambridge, 1997).

[51] A. S. Kheifets, Dynamic scaling of photo-double-ionization to electron impact, Phys. Rev. A **101**, 032701 (2020).

[52] S. L. Carter and H. P. Kelly, Double photoionization cross section of argon, J. Phys. B: At., Mol. Opt. Phys. **9**, L565 (1976).

[53] S. L. Carter and H. P. Kelly, Double photoionization of neon and argon, Phys. Rev. A **16**, 1525 (1977).

[54] C. Pan and H. P. Kelly, Photoionization cross sections of the Ar atom for production of singly and doubly charged ions near the $2p$ threshold, Phys. Rev. A **39**, 6232 (1989).

[55] M. Y. Amusia, in *Atomic Photoeffect*, edited by K. T. Taylor (Plenum, New York, 1990).

[56] M. Ya. Amusia, N. A. Cherepkov, L. V. Chernysheva, D. M. Davidović, and V. Radojević, Slow-electron elastic scattering on argon, Phys. Rev. A **25**, 219 (1982).

[57] M. Y. Amusia and L. V. Chernysheva, *Computation of Atomic Processes: A handbook for the ATOM Programs* (Institute of Physics Publishing, Bristol, 1997).

[58] M. C. Witthoeft, M. A. Bautista, C. Mendoza, T. R. Kallman, P. Palmeri, and P. Quinet, K-shell photoionization and photoabsorption of Ne, Mg, Si, S, Ar, and Ca, Astrophys. J. Suppl. Ser. **182**, 127 (2009).

[59] A. E. Kramida, Yu. Ralchenko, J. Reader, and NIST ASD Team, NIST Atomic Spectra Database (version 5.8) (online), National Institute of Standards and Technology, Gaithersburg, MD (2020), available at http://physics.nist.gov/asd.

[60] M. Hahn, A. Müller, and D. W. Savin, Electron-impact multiple-ionization cross sections for atoms and ions of helium through zinc, Astrophys. J. **850**, 122 (2017).

[61] J. S. Kaastra and R. Mewe, X-ray emission from thin plasmas: I. Multiple Auger ionisation and fluorescence processes for Be to Zn, Astron. Astrophys. Suppl. Ser. **97**, 443 (1993).

[62] A. S. Kheifets and I. Bray, Photoionization with excitation and double photoionization of the helium isoelectronic sequence, Phys. Rev. A **58**, 4501 (1998).

[63] U. Kleiman, M. S. Pindzola, and F. Robicheaux, Photoionization with excitation and double photoionization of the Li^+ ground $1\,^1$S state and metastable $2\,^{1,3}$S states, Phys. Rev. A **72**, 022707 (2005).

[64] B. M. McLaughlin, An R-matrix with pseudo-state approach to the single photon double ionization and excitation of the He-like Li^+ ion, J. Phys. B: At., Mol. Opt. Phys. **46**, 075204 (2013).

[65] A. Müller, A. Borovik, Jr., T. Buhr, J. Hellhund, K. Holste, A. L. D. Kilcoyne, S. Klumpp, M. Martins, S. Ricz, J. Viefhaus, and S. Schippers, Observation of a Four-Electron Auger Process in Near-K-Edge Photoionization of Singly Charged Carbon Ions, Phys. Rev. Lett. **114**, 013002 (2015).

[66] S. Schippers, M. Martins, R. Beerwerth, S. Bari, K. Holste, K. Schubert, J. Viefhaus, D. W. Savin, S. Fritzsche, and A. Müller, Near L-edge single and multiple photoionization of singly charged iron ions, Astrophys. J. **849**, 5 (2017).

[67] A. G. Kochur, V. L. Sukhorukov, A. J. Dudenko, and Ph. V. Demekhin, Direct Hartree-Fock calculation of the cascade decay production of multiply charged ions following inner-shell ionization of Ne, Ar, Kr and Xe, J. Phys. B: At., Mol. Opt. Phys. **28**, 387 (1995).

[68] Z. Liu, Q. Liu, Y. Ma, F. Zhou, and Y. Qu, Influence of orbital sets on the $Ar^+(2s^{-1})$ multiple Auger decay, Phys. Rev. A **103**, 063102 (2021).